Authigenic ferrimagnetic iron sulfide preservation due to non-steady state diagenesis: A perspective from Perseverance Drift, Northwestern Weddell Sea

Brendan Reilly[1], Michael L McCormick[2], Stefanie Brachfeld[3], and Brian A Haley[4]

[1]University of California San Diego
[2]Hamilton College
[3]Montclair State University
[4]Oregon State University

November 22, 2022

Abstract

We document magnetic mineral diagenesis with high resolution magnetic susceptibility, hysteresis, isothermal remanent magnetization, and other rock magnetic measurements through a shallow sulfate-methane transition (SMT) at Perseverance Drift-a high-accumulation rate Holocene biosiliceous Antarctic marine sediment deposit. The structure of the SMT is defined with porewater measurements from the same core, allowing direct comparison. Dissolution of the detrital (titano)magnetite assemblage, with preferential dissolution of stochiometric magnetite, occurs in the upper SMT. Higher coercivity magnetic minerals dissolve more slowly, continuing to dissolve through the entire SMT and could be a source of ferric iron for microbial respiration following exhaustion of porewater sulfate, as suggested by accumulation of porewater ferrous iron below the SMT. Superparamagnetic ferrimagnetic mineral enrichment/depletion occurs in three phases through the SMT and is coupled tightly to the availability of dissolved ferrous iron relative to dissolved sulfide. High concentrations of authigenic remanence-bearing iron sulfides, including greigite and hexagonal 3C pyrrhotite, which can be detected using remanence parameters but not in-field concentration dependent parameters, accumulate in a transient horizon at the base of the SMT during this early diagenesis, where sulfide is present but limited relative to dissolved ferrous iron. Formation of this remanence-bearing iron sulfide horizon is likely facilitated by continued iron reduction through the SMT. Non-steady state perturbations that shift the porewater profile, such as changes in carbon flux or sedimentation rate, can lead to preservation of these transient horizons, much like well documented preservation of manganese oxide layers in marine sediments following similar shifts to porewater profiles.

Hosted file

essoar.10504479.1.docx available at https://authorea.com/users/534304/articles/598442-authigenic-ferrimagnetic-iron-sulfide-preservation-due-to-non-steady-state-diagenesis-a-perspective-from-perseverance-drift-northwestern-weddell-sea

Authigenic ferrimagnetic iron sulfide preservation due to non-steady state diagenesis: A perspective from Perseverance Drift, Northwestern Weddell Sea

Brendan T. Reilly[1], Michael L. McCormick[2], Stefanie A. Brachfeld[3], Brian A. Haley[4]

[1] Scripps Institution of Oceanography, University of California San Diego, La Jolla, CA 92093, USA

[2] Biology, Hamilton College, Clinton, NY 13323, USA

[3] Earth and Environmental Studies, Montclair State University, Montclair, NJ 07043, USA

[4] College of Earth, Ocean, and Atmospheric Sciences, Oregon State University, OR 97331, USA

Abstract

We document magnetic mineral diagenesis with high resolution magnetic susceptibility, hysteresis, isothermal remanent magnetization, and other rock magnetic measurements through a shallow sulfate-methane transition (SMT) at Perseverance Drift—a high-accumulation rate Holocene biosiliceous Antarctic marine sediment deposit. The structure of the SMT is defined with porewater measurements from the same core, allowing direct comparison. Dissolution of the detrital (titano)magnetite assemblage, with preferential dissolution of stochiometric magnetite, occurs in the upper SMT. Higher coercivity magnetic minerals dissolve more slowly, continuing to dissolve through the entire SMT and could be a source of ferric iron for microbial respiration following exhaustion of porewater sulfate, as suggested by accumulation of porewater ferrous iron below the SMT. Superparamagnetic ferrimagnetic mineral enrichment/depletion occurs in three phases through the SMT and is coupled tightly to the availability of dissolved ferrous iron relative to dissolved sulfide. High concentrations of authigenic remanence-bearing iron sulfides, including greigite and hexagonal 3C pyrrhotite, which can be detected using remanence parameters but not in-field concentration dependent parameters, accumulate in a transient horizon at the base of the SMT during this early diagenesis, where sulfide is present but limited relative to dissolved ferrous iron. Formation of this remanence-bearing iron sulfide horizon is likely facilitated by continued iron reduction through the SMT. Non-steady state perturbations that shift the porewater profile, such as changes in carbon flux or sedimentation rate, can lead to preservation of these transient horizons, much like well documented preservation of manganese oxide layers in marine sediments following similar shifts to porewater profiles.

Key Points

- Magnetic mineral diagenesis is studied in Antarctic sediments using high resolution porewater and rock magnetic data

- Magnetic mineral dissolution and authigenesis is tightly coupled to dissolved sulfide and ferrous iron concentrations
- Remanence-bearing iron sulfides form below the sulfate-methane transition and can be preserved following non-steady state diagenesis

1. Introduction

Primary sedimentary magnetic mineral assemblages reflect sediment provenance and depositional processes; however, following deposition these magnetic mineral assemblages can alter by dissolution of components of the primary detrital assemblage or through growth of new authigenic magnetic minerals (Liu et al., 2012; Roberts, 2015). Understanding magnetic mineral diagenesis is important for interpreting paleomagnetic and environmental magnetic records. Fundamentally, magnetic mineral diagenesis is driven by changes in pore water geochemistry (e.g. Canfield and Berner, 1987; Dillon and Bleil, 2006; Garming et al., 2005; Karlin and Levi, 1983; Kars et al., 2018; Larrasoaña et al., 2007; Leslie et al., 1990), which reflects microbial activity, carbon (organic or methane) flux, oxygen (and other electron acceptors) availability, and/or sedimentation rate.

Post-depositional alteration of magnetic mineral assemblages may complicate paleomagnetic data, such as by smoothing or overprinting the signal through acquisition of a chemical remanent magnetization (CRM) at depth (e.g. Jiang et al., 2001; Rowan and Roberts, 2006). This can introduce significant uncertainty to magnetostratigraphic studies as the timing and depth ranges the authigenic minerals carrying the CRM form is poorly constrained in most systems (Roberts et al., 2018b). However, for environmental magnetic studies, magnetic mineral diagenesis is tightly coupled to iron and sulfur cycling and can preserve signals of the biogeochemical history of these systems (e.g., Kars and Kodama, 2015; Tarduno, 1994). A link to paleoenviromental conditions that could drive non-steady state changes in porewater conditions can often be made using the degree of alteration tracked by magnetic measurements, with diverse applications including sea-ice conditions in the Arctic Ocean (Brachfeld et al., 2009), abrupt changes in Asian monsoon intensity (Chang et al., 2016a), discharge events in the Santa Barbara Basin (Blanchet et al., 2009), bottom water ventilation and export productivity in the eastern Mediterranean (Larrasoaña et al., 2003) and others.

To move toward a more quantitative understanding of uncertainties in paleomagnetic data and how magnetic minerals can be used to understand diagenetic histories and their relationship with paleoenvironmental changes requires further porewater and magnetic observations from a wide range of depositional environments. Here we document how the magnetic properties of rapidly accumulating biosiliceous hemipelagic Antarctic sediments evolve in relation to sediment porewater geochemistry. The sediments studied in detail here were deposited during the latest Holocene (~800 cal yrs B.P. to present, Kyrmanidou et al., 2018) which limits the recording of environmental (and related depositional) variability associated with changes in Earth's orbit that often influence other records of paired porewater and magnetic variations (e.g. Dillon and Bleil, 2006; Garming et al., 2005).

2. Geologic Background

### 2.1 Perseverance Drift, Northeastern Antarctic Peninsula

Perseverance Drift is located north of Joinville Island on the continental shelf, Northeastern Antarctic Peninsula/Northwestern Weddell Sea, in the Joinville-D' Urville Trough (**Figure 1**). The deposit was first surveyed in 2004 by the R/V *Laurence M. Gould* (cruise LMG0404) to investigate if sediment drifts form when tidal/geostrophic currents slow at channel openings on the Antarctic shelf (Domack and the LMG0404 Scientific Party, 2004). Two Kasten cores (1.5 to 6 m, large volume, and square cross section gravity corers that are designed to preserve the sediment water interface; Kuehl et al., 1985), Cores KC3 and KC16, were recovered during this expedition (Darley, 2014). In 2012 as part of the Larsen Ice Shelf System Antarctica (LARISSA; Wellner et al., 2019) program, the R/V *Nathaniel B. Palmer* (cruise NBP1203) revisited the drift and conducted a more extensive (although incomplete due to weather and time limitations) multi-beam and sub-bottom acoustic survey, which revealed a complex seafloor with sediment thicknesses of at least 90 m (Kyrmanidou et al., 2018; Vernet and the NBP1203 Scientific Party, 2012). A Jumbo Kasten Core (JKC36; 529 cm; 63.089 °S, 55.395 °W; 806 m water depth) and Jumbo Piston Core (JPC36; 2399 cm; 63.089 °S, 55.399 °W; 806 m water depth) were recovered during this expedition. The NBP1203 geophysical survey indicates that while Cores KC3, JKC36, and JPC36 were taken from the drift, Core KC16 was recovered from a nearby sedimentary basin separate from the drift (Vernet and the NBP1203 Scientific Party, 2012).

Ice flowed over the Joinville-D' Urville Trough during the Last Glacial Maximum (Lavoie et al., 2015) and following deglaciation sediments accumulated at high rates, averaging ~760 cm/kyr for the last ~3.3 ka at the Core JKC36/JPC36 location, and provides an ultra-high resolution archive of Holocene paleoenvironmental and palaeoceanographic conditions with abundant carbonate shells for establishing a geochronology (Kyrmanidou et al., 2018). For the last three millennia, diatom assemblages reflect high primary productivity, mostly without nutrient limitation, and benthic foraminifera assemblages are consistent with high primary productivity with variable sea ice cover (Kyrmanidou et al., 2018). Benthic foraminifera assemblages suggest a paleoceanographic change at ~1.8 ka to colder conditions with more sea ice, which is interpreted as the onset of Neoglacial conditions for the Northeasternmost Antarctic Peninsula (Kyrmanidou et al., 2018).

Perseverance Drift sediments also contain the authigenic mineral ikaite ($CaCO_3 \bullet 6H_2O$), which becomes glendonite after loss of hydration and is often used as a paleoenvironmental indicator (e.g., Spielhagen and Tripati, 2009). Ikaite is found in some organic-rich biosiliceous sediments around the North/Northeastern Antarctic Peninsula at sites in the path of water masses exported from the Weddell Sea, including: the Bransfield Basin, Firth of Tay, and Vega Drift; but notably not the Palmer Deep nor western Antarctic Peninsula inner shelf deposits (Domack et al., 2007; Lu et al., 2012; Suess et al., 1982; Zhou et al., 2015). Based on modern observations, ikaite formation is associated with cold (≤10 °C) bottom waters and high porewater phosphate concentrations (Zhou et al., 2015). The latter may be related to organic matter remineralization, or, as is hypothesized for other Northeastern Antarctic Peninsula sites, may be released during Fe-bearing mineral dissolution (Zhou et al., 2015).

2.2 Magnetic Mineral Diagenesis at the Sulfate Methane Transition

Significant magnetic mineral dissolution can occur at shallow depths in marine sediments at the sulfate-methane transition (SMT) where downward diffusion of seawater sulfate (SO_4^{2-}) is used as an electron acceptor to fuel anaerobic oxidation of methane (AOM and CH_4) (Knittel and Boetius, 2009) (Equation 1). This reaction produces elevated hydrogen sulfide (HS^-) concentrations when dissolved ferrous iron (Fe^{2+}) is limited, and leads to the dissolution of iron minerals like (titano-) magnetite ($Fe_{3-x}Ti_xO_4$, which is a possible reservoir for ferric iron (Fe^{3+}) as long as x < 1) after exhaustion of more reactive species of iron (Canfield, 1989; Canfield and Berner, 1987) (Equation 2).

$$CH_4 + SO_4^{2-} \rightarrow HCO_3^- + HS^- + H_2O \;[1]$$
$$Fe^{2+} + HS^- \rightarrow FeS + H^+ \;[2]$$
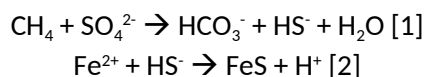
In anoxic sediments with a SMT, AOM may be the principal driver of the sulfate$^-$ profile, but sulfate reduction also occurs following the use of oxygen, nitrate, manganese, and iron as electron acceptors in the oxidation of organic carbon (Froelich et al., 1979) (Equation 3).

$$Organic\ Matter + SO_4^{2-} \rightarrow CO_2 + NH_3 + HS^- + H_3PO_4 + H_2O \;[3]$$
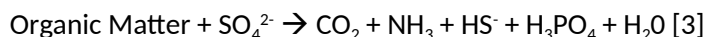
Generally, detrital magnetic mineral dissolution can be identified by a large decrease in concentration dependent magnetic parameters (referred to here as a dissolution front) and a coarsening of bulk magnetic 'grain-size' parameters, due to the preferential dissolution of finer magnetite (e.g. Karlin and Levi, 1983; Rowan et al., 2009). Additionally, following complete reduction of SO_4^{2-} and reaction of the product, HS^-, with iron to form paramagnetic pyrite (FeS_2) (Berner, 1984, 1970), HS^- could become limited with respect to Fe^{2+} in systems where there is continued dissolution of iron-bearing minerals. This geochemical setting is hypothesized to provide conditions suitable to preserve intermediaries along the pyrite formation pathway, including the ferrimagnetic mineral greigite (Fe_3S_4) (Blanchet et al., 2009; Hunger and Benning, 2007; Kao et al., 2004; Roberts et al., 2011; Rowan et al., 2009) and/or hexagonal 3C pyrrhotite. Both minerals have distinct room temperature magnetic remanence properties, despite early assumptions of the latter only having antiferromagnetic properties (Horng, 2018; Horng and Roberts, 2018). The depths at which these magnetic iron sulfides form relative to the SMT is still poorly understood (Roberts et al., 2018b).

3. Methods and Materials

3.1 Core NBP1203 JKC36

Core JKC36 was collected from Perseverance Drift using a 6 m Jumbo Kasten Corer. Upon recovery, Core JKC36 smelled strongly of H_2S and degassed CH_4, suggesting a shallow SMT that motivated this study and careful sampling by the NBP1203 shipboard geomicrobiology group. Environmental magnetic samples were taken on ship soon after collection of pore water samples and before the sediments altered significantly from warmer temperatures and oxygen exposure.

155   Core JKC36 consists of diatomaceous mud containing mm-scale laminations, streaks, and
156   patches of dark organic materials from 0 – 350 cm below sea floor (cmbsf). Below 350 cmbsf the
157   sediment becomes increasingly mottled, with laminations observed at a few intervals, and increased
158   evidence for bioturbation. Beyond laminations and evidence for bioturbation, the lithology is fairly
159   consistent, excluding an interval from 193 – 203 cmbsf described as a lighter grayish olive diatomaceous
160   mud with laminae and 205 cmbsf as a moderate olive brown silty mud with sharp contacts. Calcareous
161   shells and shell fragments are abundant but are only documented in the uppermost 50 cm of the core
162   and below 300 cmbsf. Macroscopic authigenic ikaite crystals were found at 303-305 cmbsf, 463-465
163   cmbsf, 479-481 cmbsf, and 505 cmbsf (**Figure 2**). [210]Pb dating indicates that the Kasten Corer recovered
164   an intact sediment-water interface, with little, if any, sediment lost (Kyrmanidou et al., 2018).

165

166   3.2 Sediment Magnetism

167   While on ship, 1 cm horizon samples were taken from JKC36 at 1 cm intervals from 0 to 20
168   cmbsf and at 2 cm intervals from 20 to 519 cmbsf and kept cool by refrigeration or ice packs until the
169   samples could be freeze-dried at Montclair State University. 150-300 mg of the sediment were packed
170   into gelatin capsules. Low field, mass normalized magnetic susceptibility (χ_{lf}) was measured three times
171   and averaged using an AGICO KLY-4 Kappabridge at an applied field of 300 A/m. Thermomagnetic curves
172    $\chi(T)$ were also measured for bulk sediment samples with the Kappabridge in an argon atmosphere,
173   heating from room temperature at a rate of 0.2 °C/s to ~700 °C and then cooling to ~40 °C. Select
174   intervals were measured again in ambient air without an argon atmosphere, to compare magnetic
175   mineral alteration at high temperatures. The argon atmosphere thermomagnetic curves were unmixed
176   using the method of Reilly et al. (2016), which adapts the method of Heslop and Roberts (2012) and uses
177   the Simplex Identification via Split Augmented Lagrangian (SISAL) method of Bioucas-Dias (2009). The
178   method was modified to unmix the measured curves rather than the derivative of that curve due to the
179   noisier nature of these weakly magnetic sediments and includes both heating and cooling curves. End
180   members were determined from 100 iterations with each iteration using 16 of the 18 curves to quantify
181   uncertainty associated with any one sample having too large an influence on the analysis.

182   Magnetic hysteresis parameters were measured using a Princeton Measurements Corporation
183   MicroMag 3900 vibrating sample magnetometer (VSM) with a peak 1 T field (H). The raw hysteresis
184   loops were mass-normalized and a high-field slope correction was calculated between 0.7 and 1 T.
185   Measurement averaging times were chosen based on sample raw magnetization (M) in a 1 T field,
186   ranging from 0.25 to 1 s. The bulk coercivity (H_c), saturation remanent magnetization (M_r), saturation
187   magnetization (M_s), and mass normalized high field susceptibility (χ_{hf}) were determined from these
188   loops. The VSM was also used to measure DC demagnetization of remanence curves, using an initial
189   saturation field of 1 T and an increasing incremental back-field H in -10 mT steps, with the coercivity of
190   remanence (H_{cr}) determined from where M=0 on the curve. S-ratios (Stober and Thompson, 1979) and
191   HIRMs (Stoner et al., 1996) were calculated by measuring isothermal remanent magnetizations (IRM) on
192   the VSM after applying a 1 T field and then a backfield of -0.3 T, with S-ratio = -$IRM_{-0.3T}$/IRM_{1T} and HIRM =
193   (IRM_{1T} + $IRM_{-0.3T}$)/2. First order reversal curves (FORCs; n = 140 per sample; Pike et al., 1999) were
194   measured on the VSM for selected samples using a 0.5 T saturating field, 0.25 s averaging time, H_b range
195   of -30 mT to 30 mT, and H_c range of 0 to 100 mT. FORCs were processed using FORCinel v. 3.03 software
196   (Harrison et al., 2018; Harrison and Feinberg, 2008) and VariFORC smoothing (Egli, 2013).

197   IRM acquisition was measured for selected gelatin capsules following demagnetization with a
198   200 mT peak alternating field (AF) using an ASC Scientific D-2000 AF demagnetizer. Stepwise IRM was
199   imparted using an ASC Scientific IM-10-30 Impulse Magnetizer and measured on an AGICO JR-6 spinner
200   magnetometer at 50 mT intervals from 0 to 0.3 T, 100 mT intervals from 0.3-1 T, and 1 T intervals from
201   1-5 T.

202   Low temperature measurements were made with a Quantum Design Magnetic Properties
203   Measurement System (MPMS) at the Institute for Rock Magnetism, University of Minnesota. Field
204   Cooled (FC) remanence measurements were made by cooling the sample to 20 K in a 2.5 T field and
205   measuring the magnetization at ~5 K intervals as the sample warmed to 300 K. Zero Field Cooled (ZFC)
206   remanence measurements were made with the same protocol, except the sample was cooled to 20 K in
207   zero applied field. MPMS magnetic susceptibility ($\chi_{lf\text{-}MPMS}$) was measured as a function of temperature
208   and field frequency at ~10° increments during warming from 20 K to 300 K, with an applied field of 240
209   Am^{-1} at 5 frequencies (1, 5.6, 31.6, 177.6, and 997.3 Hz). Frequency dependent magnetic susceptibility
210   (χ_{FD}), reported as a percent, was calculated as the difference between $\chi_{lf\text{-}MPMS}$ at 31.6 and 1 Hz,
211   normalized by the $\chi_{lf\text{-}MPMS}$ at 1 Hz.

212   To complement the magnetic analyses, heavy mineral extracts were prepared from bulk freeze-
213   dried sediment at 0, 148, 206, and 450 cmbsf through centrifuging in a sodium polytungstate solution
214   with a density of 2.88 g/cm^3 and freezing with dry ice (Skipp and Brownfield, 1993). Heavy mineral
215   extracts were mounted on carbon tape and were carbon coated for imaging using a Hitachi S-3400N
216   scanning electron microscope (SEM) and for qualitative chemical analysis on a Bruker X-flash energy
217   dispersive spectrometer (EDS), using a 15 keV accelerating voltage.

218   To compare sediment magnetic properties with those of potential source rocks, 23 bedrock
219   samples were chosen from the Polar Rock Repository (PRR) at the Byrd Polar Research Center, Ohio
220   State University, that were proximal to our study area (Joinville Island and nearby smaller islands) and
221   which attempt to represent regional lithologies, including sedimentary, volcanic, and intrusive igneous
222   samples. Rock chips (~50-150 mg) were immobilized with quartz Fiberfrax® inside gelatin capsules and
223   were measured for χ_{lf} and hysteresis parameters in the same fashion as for the Core JKC36 sediments.
224   All PRR sample high temperature χ_{lf} measurements were made in an argon atmosphere.

225

226   ### 3.3 Porewater Geochemistry
227   Subcores for porewater geochemical analysis were collected from target depths immediately
228   after removing each Jumbo Kasten Core panel. Duplicate sediment samples for CH_4 analysis (1 mL each)
229   were collected with sterile 3 mL pre-cut open-end syringes and transferred to N_2 purged 10 mL gas
230   chromatography (GC) vials pre-filled with 2 mL of 1 M NaOH then capped and sealed with teflon-coated
231   butyl rubber septa. Vials were equilibrated at 30 °C for 30 minutes then analyzed by manual headspace
232   sampling and injection on a shipboard Agilent 6890N gas chromatograph using a Plot-Q column and
233   flame ionization detection (FID). Final concentrations were corrected for porewater content (mL H_2O/
234   mL sediment).

235   All other samples for porewater analysis were collected in sterile 60 mL pre-cut open-end
236   syringes. Immediately after recovery, syringes were wrapped in parafilm and vinyl tape and were
237   transferred to a N_2 purged glove box maintained at 1 °C for subsampling. All remaining manipulations

238   were conducted in a glove box. Sediment was transferred to gas-tight acid-washed polycarbonate Oak

239   Ridge tubes and centrifuged at 10,000 RCF for 20 min at 4 °C. The supernatant was collected and filtered

240   through a 0.22 µm polyethersulfone syringe filter and aliquoted for sulfide, sulfate and ferrous iron

241   assays. Sulfide samples were preserved by equal volume addition to anoxic 20% Zn acetate solution and

242   later quantified colorimetrically by the Cline method (Cline, 1969). Samples for sulfate and other anions

243   were stored at 4 °C in the dark until analyzed by ion chromatography on a Metrohm 861 Advanced

244   Compact IC unit using a Metrosep A SUPP 5-250/4.0 anion column. Samples for Fe^{2+} (aq) were preserved

245   by equal volume dilution with 0.1 M HCl and later quantified colorimetrically by the Ferrozine assay

246   (Stookey, 1970).

247

248   4. Results

249

250   4.1 Porewater Geochemistry

251   Core JKC36 has a shallow SMT centered around 70 cmbsf, with $[SO_4^{2-}]$ declining in concentration

252   from ~23-27 mM in the upper 20 cm to background levels at 80 cmbsf. Sulfide, $[S^{2-}]$, is present above

253   background levels (> .5 mM) between 10 and 225 cmbsf with peak concentration of 6 mM. Methane,

254   CH_4, is present above background levels below 60 cmbsf (**Figure 2**). As Core JKC36 degassed methane

255   upon recovery, CH_4 levels above the solubility limit at 1 atmosphere and 0 °C (~ 2.3 mM) are highly

256   variable and reflect this degassing (Yamamoto et al., 1976). $[Fe^{2+}]$ is present in high concentrations (~6

257   µM) at the core top but decreases in the upper 10 cm to background levels between 10 and 80 cmbsf,

258   where sulfate is actively reduced and sulfide accumulates in the porewater. Between 80 and 180 cmbsf,

259    $[Fe^{2+}]$ is elevated, despite the presence of $[S^{2-}]$ in the porewater, with peak concentrations (~3 µM) at

260   140 cmbsf. Below 180 cmbsf, $[Fe^{2+}]$ returns to background levels.

261   AOM coupled to microbial sulfate reduction is likely occurring between 60 and 80 cmbsf, where

262    $[SO_4^{2-}]$ and CH_4 are both present in the porewater (**Figure 2**). Accumulation of $[Fe^{2+}]$ directly below the

263   exhaustion of sulfate, suggests that iron reduction is also occurring within the SMT. This iron reduction

264   must be occurring at a rate where $[Fe^{2+}]$ is being produced faster than it can react with $[S^{2-}]$. Iron

265   reduction at and below the SMT could be explained by iron dependent AOM, which uses ferric iron

266   instead of sulfate as an electron acceptor (Beal et al., 2009; Riedinger et al. ,2014).

267

268   4.2 Sediment Magnetism

269

270   4.2.1 Concentration Dependent Magnetic Parameters

271   The χ_{lf} profile for Core JKC36 is marked by a steady decline in values (~10 to 7 x 10^{-7} m^3/kg) in the

272   upper 30 cm and a sharp drop-off immediately below that, consistent with dissolution fronts described

273   in sulfate reducing sediments (e.g. Karlin and Levi, 1983; Rowan et al., 2009) (**Figure 3**). This dissolution

274   front is also observed in the concentration dependent parameter M_s, which tracks the total in-field

275   ferrimagnetic saturation magnetic moment, and M_r, which tracks the total remanent ferrimagnetic

276   moment. The dissolution front observed in these three parameters occurs in the upper portion of the

277   SMT when $[S^{2-}]$ is only about one-third of the highest measured concentration (~2.3 mM). Below the

278 dissolution front, χ_{lf}, M_s, and M_r have high frequency variability (on the order of 10-20 cm), with a shift
279 from relatively lower mean values (χ_{lf} = 4.1 x 10^{-7} m^3/kg) to higher mean values (χ_{lf} = 5.0 x 10^{-7} m^3/kg)
280 around 330 cmbsf.

281   The χ_{hf} profile tracks the non-ferrimagnetic contributions to magnetic susceptibility and, under
282 ideal circumstances, reflects the relative proportion of paramagnetic minerals (often iron-bearing) to
283 diamagnetic minerals. In reality, χ_{hf} must be interpreted with caution because if high-coercivity minerals
284 are present, like hematite and goethite, which saturate in fields above 700 mT, their induced
285 magnetization can influence the slope of the magnetization as a function of field strength and therefore
286 the calculation of χ_{hf} (Brachfeld, 2006). With that in mind, χ_{hf} decreases in the upper 30 cm along with χ_{lf},
287 M_s, and M_r, which is consistent with steady dissolution of iron-bearing paramagnetic minerals along with
288 ferrimagnetic minerals above the dissolution front (**Figure 3**). However, there is no sharp dissolution
289 front in the χ_{hf} profile like that observed in the χ_{lf}, M_s, and M_r profiles. Also, unlike χ_{lf}, M_s, and M_r, the χ_{hf}
290 values increase after a minimum around 48 cmbsf and reach a local maximum around 98 cmbsf, where
291 $[S^{2-}]$ also reaches its highest measured value. This is consistent with the formation of new authigenic
292 paramagnetic minerals—likely pyrite. Below this horizon, χ_{hf} undergoes high frequency variation without
293 the increase around 330 cmbsf, as was observed in χ_{lf}, M_s, and M_r. There is a peak in χ_{hf} at 206 cm;
294 however it is difficult to know if this is related to a higher concentration of paramagnetic minerals or an
295 artifact of the higher concentration of high-coercivity minerals at the same horizon, discussed below.

296   HIRM values, which track the concentration of minerals that contribute to magnetic remanence
297 with coercivities greater than 300 mT, are about two orders of magnitude lower than M_r values, which
298 track the total magnetic remanence of the sediments (median values are 4.2 x 10^{-5} versus 2.5 x 10^{-3} Am^2/
299 kg, respectively; **Figure 3**). This suggests that to first order, X_{lf}, M_s, M_r largely reflect lower coercivity
300 ferrimagnetic mineral concentrations. HIRM values do not decrease significantly in the upper 30 cm like
301 the other concentration dependent parameters. However, HIRM values decline steadily below the χ_{lf},
302 M_s, and M_r dissolution front to a local minimum around 174 cmbsf, near the base of the SMT, which
303 suggests continued steady dissolution of minerals with coercivities greater than 300 mT through the
304 entire interval of elevated $[S^{2-}]$, including following the exhaustion of $[SO_4^{2-}]$ around 80 cmbsf and
305 accumulation of $[Fe^{2+}]$ below that (**Figure 2**). This is consistent with other diagenetic environments,
306 where high coercivity minerals like hematite that may be a minor contributor to the magnetization of
307 the primary detrital assemblage dissolve more slowly than (titano)magnetite (Dillon and Bleil, 2006;
308 Garming et al., 2005; Liu et al., 2004; Yamazaki et al., 2003) and implies that these high-coercivity
309 minerals are likely a source of ferric iron within the SMT for iron reduction.

310   Starting at the base of the SMT, HIRM values (> ~1 x 10^{-4} Am^2/kg) indicate horizons with
311 enrichments of magnetic minerals with coercivity greater than 300 mT, particularly at 206 cmbsf and
312 442 cmbsf (up to 5.5 and 1.2 x 10^{-4} Am^2/kg, respectively; **Figure 3**). These horizons have sharp bases and
313 grade upward to lower HIRM values. The 206 cmbsf horizon reaches HIRM values an order of magnitude
314 greater than underlying or overlying sediments and is accompanied by a spike in M_r values (up to 9.6 x
315 10^{-3} Am^2/kg), but it is not detected in χ_{lf} or M_s. This suggests that the enrichment of this high coercivity
316 mineral contributes significantly to magnetic remanence but does not reach high enough concentrations
317 to be detected using in-field concentration dependent measurements in the presence of the background
318 ferrimagnetic mineral assemblage.

319

4.2.2 High Temperature Magnetic Susceptibility

χ_{lf} as a function of heating to ~700 °C and cooling back to room temperature has variable behavior with the most pronounced difference being that cooling curves are always weaker than or about equal to heating curves from 0-30 cmbsf (above the dissolution front). Cooling curves are generally stronger than heating curves below the dissolution front (**Figure 4a**). Principal component analysis of the χ_{lf} temperature curves indicates that the first and second components explain about 86% and 7% of the variance, respectively, with significantly less variance explained by subsequent components. Accordingly, we adopt a 3 end-member solution using a regularization parameter (τ) of 0.7848, which is the value that uses that smallest simplex that still has a good fit to the data (**Figure 4e**) (see Reilly et al. (2016) for discussion).

The composition of the surficial sediments (0 cmbsf) is almost entirely composed of end-member 1 (EM1) and EM1 is likely representative of the primary detrital magnetic mineral assemblage. It is the only end-member with a cooling curve weaker than the heating curve, which suggests the presence of maghemite, which inverts to hematite at high temperatures (Gehring et al., 2009; Özdemir and Banerjee, 1984) (**Figure 4d**). χ_{lf} increases with initial heating starting with a relatively slow increase at around 150 °C and increasing to a relatively faster rate around 230 °C. Peak χ_{lf} is achieved at around 300 °C, after which it steadily decreases until about 557 °C, where it begins a sharp drop centered at around 580 °C. This is the only end-member with a pronounced decline at about 580 °C, which suggests that EM1 is the only end-member with a significant proportion of stochiometric magnetite. The cooling curve has about the same slope as the heating curve while cooling from 550 and 350 °C, which suggests that the gradual χ_{lf} decline in this temperature range is related to the presence of titanomagnetite of variable titanium concentrations (Lattard et al., 2006).

End-members 2 (EM2) and 3 (EM3) have similar heating curves, with only a slight χ_{lf} increase between 200 and 300 °C and a steady decline between about 350 and 600 °C with no sharp drop-offs (**Figure 4d**). Cooling curves generally retrace the heating curve during cooling to about 500 °C and then have stronger χ_{lf} than the heating curve while cooling to room temperature. The major difference between EM2 and EM3 is that EM3 has a sharp χ_{lf} increase on cooling centered around 265 °C with a maximum χ_{lf} at about 233 °C and decrease in χ_{lf} as it continues to cool, suggesting alteration in EM3 samples that does not occur in EM2 samples. This could be indicative of the creation of an antiferromagnetic hexagonal pyrrhotite polytype during heating, one that is only ferrimagnetic between its λ transition ~200-220 °C and its Curie temperature of ~275-295 °C. We note this polytype is different from the hexagonal 3C pyrrhotite with room temperature ferrimagnetic properties (Horng, 2018) discussed elsewhere in this study. This interpretation is consistent with previously published reports of pyrrhotite polytypes produced during the alteration of greigite and other iron sulfides at high temperatures or under oxic conditions (Chang et al., 2008; Roberts et al., 2011; Schwarz and Vaughan, 1972; Sweeney and Kaplan, 1973).

Downcore variability in the end-member abundances suggest that the EM1 primary ferrimagnetic mineral assemblage (or as close to the primary assemblage as the 0 cmbsf sample captures), contains stochiometric magnetite, maghemite, and titanomagnetite with a range of compositions. EM1 steadily decreases in its relative abundance from 0 to 30 cmbsf, above the dissolution front, along with the steady decrease in room temperature χ_{lf}, which suggests that dissolution through this interval is preferentially removing stochiometric magnetite and maghemite relative to titanomagnetite (**Figure 4b-c**). A preference for dissolution of stochiometric magnetite over

363 titanomagnetite has been observed elsewhere in diagenetic sediments, likely because Ti^{4+} substitution
364 reduces the ratio of Fe^{3+} to Fe^{2+} in the mineral (Dillon and Bleil, 2006). There is no clear trend in end-
365 member abundance below the dissolution front nor in end-member abundances where there is elevated
366 pore water [S^{2-}], but the ferrimagnetic assemblages are dominated by titanomagnetite with or without
367 mineral phases that alter to an antiferromagnetic hexagonal pyrrhotite polytype. Enrichment of the EM3
368 assemblage that contains the mineral phases that alter to an antiferromagnetic hexagonal pyrrhotite
369 polytype often coincides with HIRM peaks (**Figure 3**).

370

371 ### 4.2.3 Concentration Independent Magnetic Parameters
372 Concentration independent magnetic parameters can be influenced by relative changes in
373 magnetic coercivity and magnetic mineralogy. Hysteresis loop ratios M_r/M_s and H_{cr}/H_c are often
374 interpreted as reflecting changes in magnetic grain-size or domain state (e.g. Day et al., 1977); however,
375 they can also be influenced by variations in relative proportions of magnetic mineralogy, surface
376 oxidation, and numerous other factors (e.g. Roberts et al., 2018a). As we have already documented
377 differences in relative magnetic mineralogical abundances during diagenesis in the SMT (**Figures 3 and
378 4**), we keep this in mind in our discussion of concentration independent magnetic parameter. For
379 discussion, we divide the core into five zones based on magnetic mineral parameters (particularly M_s
380 and H_{cr}/H_c) and porewater geochemistry variations.

381 Zone 1 (0-33 cmbsf) represents the interval from the top of the core to the base of the
382 dissolution front, during the initial downcore [S^{2-}] rise in the upper portion of the SMT (**Figure 5a**). The
383 change in magnetic mineral concentration in this interval, tracked by M_s, has a strong correlation with
384 M_r/M_s (r = 0.83), H_{cr}/H_c (r = -0.94), and S-ratio (r = 0.95) but a weak correlation with H_{cr} (r = 0.34) (**Figures
385 5**). This reflects 'coarsening' of the magnetic mineral assemblage due to preferential dissolution of fine
386 magnetic minerals. The absence of a trend in the H_{cr} values and significant correlation with S-ratio, also
387 reflects mineralogic changes. The lack of H_{cr} trend above the dissolution front could reflect the
388 competing influence of dissolution of stable single domain magnetite, lowering the coercivity of
389 remanence-bearing minerals and preferential preservation of titanomagnetite (**Figure 4c**), and slower
390 dissolution of high coercivity minerals (**Figure 3**), which increases the bulk coercivity of remanence.

391 Zones 2a (33-87 cmbsf) and 2b (87-131 cmbsf) represent the interval of peak [S^{2-}]. Zone 2a has
392 increasing sulfide downcore, decreasing sulfate, and low [Fe^{2+}], which indicate that sulfate reduction is
393 producing more [S^{2-}] than can react with [Fe^{2+}]. Zone 2b has decreasing [S^{2-}] downcore, depleted [SO_4^{2-}],
394 and elevated [Fe^{2+}], which indicate that there is enough [Fe^{2+}] to react with the [S^{2-}] (**Figure 2**). While M_r/
395 M_s and H_{cr} values are comparable for both Zones 2a and 2b, H_{cr}/H_c values are distinct—driven by H_c
396 variability (means and ranges for these parameters are shown in **Figure 5b**). H_{cr} is a remanence
397 measurement and H_c is an in-field measurement, so the variability in H_c and lack of variability in H_{cr} is
398 likely driven by the concentration of superparamagnetic (SP) minerals that lower the bulk coercivity in
399 the presence of a magnetic field with evidence for SP enrichment in Zone 2a but not 2b. This
400 observation suggests that the concentration of SP minerals in the SMT is strongly related to the
401 availability of [S^{2-}] relative to [Fe^{2+}].

402 The relationship between magnetic mineral concentration, tracked by M_s, and concentration
403 independent parameters changes in Zone 2a and 2b relative to Zone 1, with M_r/M_s (r = -0.57 and -0.78,

404 respectively) and H_{cr} (r = -0.75 and -0.78) having strong negative correlations, and S-ratio and H_{cr}/H_c
405 having much weaker correlations than Zone 1. Thus, rather than a coercivity 'coarsening' with decreases
406 in ferrimagnetic concentration as is observed above the dissolution front in Zone 1, below the
407 dissolution front in Zones 2a and 2b there is a coercivity 'fining' of the ferrimagnetic particles with
408 decreases in ferrimagnetic concentration.

409   Zones 3a (131-329 cmbsf) and 3b (329-519 cmbsf) represent the interval at the base of the SMT
410 and the underlying methanic zone. In general, M_r/M_s, H_{cr}/H_c, and H_{cr} values are like those found in Zone
411 2a, which suggests an altered magnetic mineral assemblage, like that found beneath the dissolution
412 front, and variable SP concentrations (**Figure 5**). Horizons previously discussed at 206 and 442 cmbsf
413 with high HIRM values (**Figure 3**) are characterized by high M_r/M_s, H_c, and H_{cr} values and low S-ratio
414 (**Figure 5**). When plotting M_r/M_s versus H_{cr}/H_c on a Day Plot (Day et al., 1977), these anomalous
415 mineralogy intervals are characterized by the looping pattern often documented in sulfate reducing
416 sediments (Rowan et al., 2009; Yamazaki et al., 2003). This has been interpreted as due to the
417 enrichment of SP grains pushing values to higher H_{cr}/H_c values, and then increased abundance of single
418 domain magnetic minerals increasing M_r/M_s while decreasing H_{cr}/H_c (**Figure 5b**). When M_r/M_s is plotted
419 against H_{cr}, the looping pattern disappears, and the values plot along a single mixing relationship
420 between the high M_r/M_s and H_{cr} and low M_r/M_s and H_{cr} values, which supports the interpretation that
421 the looping pattern caused by H_{cr}/H_c variation is driven by the abundance of SP grains influencing the in-
422 field parameter (H_c) and not the remanence parameter (H_{cr}). Unlike prior interpretations, H_{cr} values are
423 higher and S-ratio values are lower for the high coercivity horizons at 206 and 442 cmbsf than might be
424 expected from the addition of authigenic greigite alone (Horng, 2018). In other environments, similar
425 horizons with low S-ratios have been attributed to pyrrhotite (Kars and Kodama, 2015) and
426 measurements of a variety of magnetic iron sulfides suggest that these coercivities could be explained as
427 a mixture of the altered detrital assemblage observed above and below this horizon and authigenic
428 hexagonal 3C pyrrhotite (Horng, 2018).

429   Zone 3b is different than Zone 3a in that it has higher concentrations of ferrimagnetic minerals,
430 as indicated by χ_{lf}, M_s, and M_r, lower coercivity of remanence bearing minerals, as indicated by M_r/M_s
431 and H_{cr}, and lower proportions of high-coercivity (>300 mT) minerals, as indicated by higher S-ratios
432 (**Figures 5**). [S^{2-}] and [Fe^{2+}] are negligible at these depths, so this less-altered magnetic mineral
433 assemblage potentially reflects a preserved signal of past diagenetic conditions.

434

435 4.2.4 Detailed Rock Magnetic Investigations
436

437 *4.2.4.1 First order reversal curves (FORCs)*
438   FORCs were measured to investigate the primary magnetic mineral assemblage (0 cmbsf), the
439 altered assemblage in the lower half of the SMT (148 cmbsf), the altered assemblage well below the
440 SMT in the methanic zone (458 cmbsf), and at the anomalous magnetic mineral horizon recognized by
441 high values of HIRM and remanence sensitive parameters (i.e., M_r, M_r/M_s, H_c, and H_{cr}) and low S-ratio
442 values (206 cmbsf) (**Figures 3 and 5**). The 0 cmbsf sample has a signature consistent with a primary
443 detrital assemblage that consists of a range of magnetic domain states, including single domain and
444 vortex state grains, while the 148 and 458 cmbsf samples display lower coercivities consistent with a mix

445   of vortex state, multidomain, and possibly SP grains (**Figure 6a**). Compared with FORC diagrams from
446   other sulfidic sediments, neither the 148 nor the 458 cmbsf sample are consistent with FORC signatures
447   for pure SP/single domain greigite or hexagonal 3C pyrrhotite (Roberts et al., 2018b); however, if those
448   minerals are present they may not be easy to recognize if they exist in a mixture with the altered
449   primary detrital assemblage. Comparison of the primary detrital assemblage (0 cmbsf) and the altered
450   assemblage (148 and 458 cmbsf) suggests that magnetic mineral dissolution in the SMT primarily
451   removed the finest single-domain to vortex state grains from the primary assemblage.

452   The 206 cmbsf sample has a FORC distribution that extends to higher H_c with a tighter
453   distribution around the H_u = 0 mT axis, but still contains some spread indicating magnetostatic
454   interactions. This FORC diagram likely represents a mixture of the altered detrital assemblage (± SP
455   grains) observed in the 148 cmbsf and 458 cmbsf samples and an anomalous higher coercivity magnetic
456   mineral assemblage. Compared with FORC diagrams from other sulfidic sediments, this assemblage is
457   consistent with a mixture of the altered detrital assemblage observed in the 148 and 458 cmbsf samples,
458   SP/single domain greigite, and another mineral with coercivity higher than typical examples of greigite
459   bearing samples (Roberts et al., 2018b). The FORC distribution is somewhat skewed to more negative H_u
460   values in the 40 – 80 mT H_c range and extends beyond the measured H_c range that could indicate fine
461   grained and/or authigenic sedimentary 3C pyrrhotite contribution to the coercivity distribution of the
462   206 cmbsf sample (Horng, 2018). We note that the 206 cmbsf has differences from past examples of
463   pyrrhotite interpreted to be present in diagenetic sediments (e.g., Horng, 2018; Kars and Kodama, 2015;
464   Larrasoaña et al., 2007), which we attribute to the mixture of detrital and authigenic minerals in the
465   sample. While hematite could also explain the high coercivities (Roberts et al., 2006), this would require
466   a high weight percentage of hematite relative to the lower coercivity phases, which is inconsistent with
467   no apparent decrease ~670 $^{\circ}$C in the high temperature χ_{lf} curves (Carvallo et al., 2006; Liu et al., 2019).

468

469   *4.2.4.2 Isothermal remanent magnetization (IRM) acquisition*
470   IRM acquisition curves were measured at or near the same intervals at the FORC diagrams to
471   further investigate the coercivities of the remanence bearing grains. IRM values at each acquisition step
472   are reported after being normalized by the IRM acquired at 1 T, as IRMs measured above 1 T were
473   imparted using a different coil and have slightly lower values than those collected at 1 T and below.
474   There is no significant remanence acquisition from 2 to 5 T for any samples.

475   The 0, 148, and 450 cmbsf IRM acquisition curves are similar, which was expected with S-ratio
476   values from 0.96 to 0.99. The initial acquisition at 50 mT is slightly lower for the 0 cmbsf sample (0.50)
477   relative to the 148 cmbsf (0.54) and the 450 cmbsf sample (0.56), but changes with the 148 and 450
478   cmbsf samples with a slightly stronger IRM acquired between 100 and 300 mT (e.g., IRMs at 150 mT are
479   0.93, 0.88, and 0.91, respectively) (**Figure 6**). All three samples reach values of at least 0.99 by the 500
480   mT step. This is consistent with the altered assemblages in the 148 and 450 cmbsf samples coarsening
481   slightly at lower coercivities, but also including greater (but still low) concentrations of a higher
482   coercivity component that saturates above 300 mT but below 500-600 mT.

483   The 206 cmbsf sample is unique in that it has a lower S-ratio (0.87) and acquires IRM more
484   slowly than the other samples, with only 0.26 acquired by 50 mT, 0.65 acquired by 150 mT, and 0.92 by
485   300 mT (**Figure 6**). However, the 206 cmbsf sample also reaches 0.99 by 500 mT, suggesting the high

486 coercivity values are driven by a mineral that saturates at fields greater than 300 mT, thus driving S-ratio
487 and HIRM variability around this horizon, but lower than about 500-600 mT. Greigite is generally
488 reported as having coercivities like that of magnetite, saturating by around 300 mT, and single domain
489 greigite has been shown to acquire a remanence faster than the 206 cmbsf sample (normalized
490 remanence of about 0.90 at 150 mT; Roberts et al., 2011). Comparison of the S-ratio of metamorphic
491 monoclinic 4C pyrrhotite (0.96-1.00), sedimentary greigite nodules (0.98-1.00), and sedimentary
492 authigenic hexagonal 3C pyrrhotite nodules (0.52-1.00), suggest the authigenic 3C pyrrhotite can be
493 distinguished from other magnetic iron sulfides based on its higher coercivity (Horng, 2018; Horng and
494 Roberts, 2018). So, the presence of greigite cannot explain the high coercivity of the 206 cmbsf sample,
495 but authigenic hexagonal 3C pyrrhotite could.

496

497 *4.2.4.3 Magnetic susceptibility (χ_{lf}) as a function of heating in argon and ambient air*
498   To further investigate if thermomagnetic curve features discussed in Section 4.2.2 and
499 presented in **Figure 4** reflect magnetic phase transitions or mineral alteration upon heating, we
500 remeasured four samples (using fresh material from the same core horizon) for χ_{lf} as a function of
501 heating to ~700 °C and cooling back to room temperature in ambient air, at or around the same intervals
502 as the FORC measurements (**Figure 6c**). The heating curves measured in ambient air are nearly identical
503 to those measured in argon atmospheres, while the cooling curves measured in ambient air at
504 temperatures less than ~450 °C are always greater than those measured in argon atmospheres. In the 0,
505 206, and 500 cmbsf ambient air thermomagnetic curves, a local χ_{lf} maximum is introduced in the cooling
506 curve between ~200 and 300 °C, which suggests that heating in ambient air facilitates alteration of a
507 mineral phase, such as greigite or other iron sulfides (Chang et al., 2008; Roberts et al., 2011; Schwarz
508 and Vaughan, 1972; Sweeney and Kaplan, 1973), to an antiferromagnetic hexagonal pyrrhotite polytype,
509 one that is different from the hexagonal 3C pyrrhotite with ferrimagnetic room temperature properties
510 (Horng, 2018, discussed elsewhere). This feature is present with similar amplitude in both the argon and
511 ambient air measurements at 100 cmbsf. The similarity of the heating curves support the earlier
512 interpretation in Section 4.2.2 that the features of the heating curves are related to magnetic phase
513 transitions and that our primary magnetic assemblage is dominated by magnetite, maghemite, and
514 titanomagnetite, which is modified during diagenesis.

515

516 *4.2.4.4 Zero field cooled (ZFC) and field cooled (FC) remanence*
517   To investigate the low temperature properties of the remanence bearing magnetic minerals we
518 measured ZFC and FC remanences at four intervals at or near where the FORC measurements were
519 made (**Figure 6d**). While these measurements are not typically considered useful for the identification or
520 characterization of potential authigenic minerals that lack low-temperature order-disorder transitions
521 like greigite (Roberts et al., 2011), they do offer an additional constraint on the magnetic mineral
522 assemblage present.

523   Low temperature data do not contain a clear phase transition at 30-34 K, as would be expected
524 for monoclinic 4C pyrrhotite (Rochette et al., 1990). However, this transition is not detected in
525 authigenic sedimentary hexagonal 3C pyrrhotite nodules, which have similar behavior to greigite in FC
526 and ZFC measurements (Horng, 2018; Horng and Roberts, 2018). A magnetization decrease is present in

527   all samples between 100 and 120 K, which is indicative of a Verwey transition in magnetite. Quantifying

528   the remanence loss using the δT_v parameter of Moskowitz et al. (1993) (δT_v = LTSIRM$_{80K}$ –

529   LTSIRM$_{150K}$/LTSIRM$_{80K}$; where LTSIRM is the field cooled low temperature saturation IRM) indicates a

530   similar remanence loss in the altered magnetic mineral assemblage for samples 100 and 450 cmbsf (δT_v

531   = 0.47 and 0.51, respectively) which is somewhat greater than for the primary magnetic mineral

532   assemblage sample at 0 cmbsf (δT_v = 0.37). The anomalous magnetic mineral assemblage at 206 cmbsf

533   has the smallest remanence decrease (δT_v = 0.21). Suppression of the Verwey transition in the primary

534   magnetic assemblage relative to the altered assemblage samples could be related to the presence of

535   oxidized maghemite, as recognized in the high temperature χ_{lf} curves (Özdemir et al., 1993). Even

536   greater suppression of the Verwey transition in the anomalous assemblage at 206 cmbsf that lacks

537   strong evidence for maghemite could be explained by the presence of populations of fine SD size

538   magnetic grains and/or greigite (Moskowitz et al., 1993) or authigenic hexagonal 3C pyrrhotite (Horng

539   and Roberts, 2018).

540   The remanence loss above the Verwey transition varies for each sample as quantified by the δM

541   parameter (δM = (LTSIRM$_{150K}$ – LTSIRM$_{300K}$)/LTSIRM$_{150K}$) (Hatfield et al., 2017; Moskowitz et al., 1998). The

542   gradual remanence decrease above the Verwey transition is smaller for the primary detrital assemblage

543   at 0 cmbsf (δM = 0.29) than for the altered assemblages in the 100 and 450 cmbsf samples (δM = 0.45

544   and 0.48, respectively). This increase in δM is consistent with the high temperature χ_{lf} data that indicate

545   an increased relative proportion of titanomagnetite to stochiometric magnetite in the altered magnetic

546   mineral assemblages. The anomalous magnetic mineral assemblage at 206 cmbsf has an intermediate

547   remanence decrease above the Verwey transition (δM = 0.37), which is likely related to the mixture of

548   the altered magnetic mineral assemblage with another magnetic mineral phase. High temperature χ_{lf}

549   behavior rules out significant stochiometric magnetite or titanomagnetite with a different composition

550   than other samples below the dissolution front. Alternative candidates could be a higher proportion of

551   iron sulfides like fine grained authigenic greigite or hexagonal 3C pyrrhotite within the altered magnetic

552   mineral assemblage, which have only a small decrease above the Verwey transition temperature (Chang

553   et al., 2009; Horng and Roberts, 2018).

554   ZFC remanence values are typically greater than FC remanence values for the primary (0 cmbsf)

555   and altered samples (100 and 450 cmbsf), but less than FC remanence values for the anomalous sample

556   at 206 cmbsf. Quantifying this difference using the R_{LT} parameter of Smirnov (2009) (R_{LT} = FC SIRM$_{20K}$/ZFC

557   SIRM$_{20K}$) yields similar values for the 0, 100, and 450 cmbsf samples (R_{LT} = 1.04, 1.06, and 1.05,

558   respectively) and a higher value for the anomalous magnetic mineral assemblage at 206 cmbsf (R_{LT} =

559   1.16), which is consistent with the presence of vortex state grains in the primary and altered

560   assemblages and fine-grained single domain grains in the 206 cmbsf sample (Smirnov, 2009). Like the

561   206 cmbsf sample, greigite and hexagonal 3C pyrrhotite samples have FC curves greater than ZFC curves

562   (Chang et al., 2008; Horng and Roberts, 2018).

563

564   *4.2.4.5 Low temperature and frequency dependence of magnetic susceptibility*

565   To further investigate the low temperature properties of the magnetic mineral assemblages, we

566   measured $\chi_{lf-MPMS}$ as a function of temperature below room temperature at a variety of frequencies for

567   three intervals representative of the primary detrital assemblage (0 cmbsf), altered detrital assemblage

568   (100 cmbsf), and anomalous assemblage (206 cmbsf) (**Figure 6e**). Frequency dependent magnetic

14

569 susceptibility ($X_{fd} = (\chi_{1\,Hz} - \chi_{31.6\,Hz})/\chi_{1\,Hz}$ x 100) is highest at 300 K for the 206 cmbsf sample and lowest for
570 the 0 cmbsf sample with the 100 cmbsf sample falling in between. These values and the increasing χ_{fd}
571 values with temperature above 100 K suggest enrichment of SP and single domain grains in the altered
572 assemblage captured by the 100 cmbsf sample and the anomalous assemblage captured by the 206
573 cmbsf sample relative to the 0 cmbsf sample (Worm, 1998; Worm and Jackson, 1999). χ_{fd} peaks between
574 about 60 and 70 K can be attributed to thermally activated electron hopping in titanomagnetite (Carter–
575 Stiglitz et al., 2006; Hatfield et al., 2017; Walz et al., 1997).

576

577 4.2.5 Scanning Electron Microscope Observation of Fe-Ti Oxides and Fe Sulfides

578   Unpolished heavy mineral extract samples representative of the altered detrital assemblage at
579 148 and 450 cmbsf and the anomalous magnetic mineral assemblage at 206 cmbsf were observed to
580 assess the potential contributors to the sediment magnetism. While it is perhaps likely that magnetic
581 mineral inclusions in silicate minerals should be considered (e.g. Chang et al., 2016b; Hatfield et al.,
582 2017), they could not be imaged with our unpolished samples. Fe-Ti oxides, when observed, have
583 evidence of surface pitting or other dissolution structures, often with iron sulfides present on the
584 mineral surface and in cavities (**Figure 7a-c**), similar to observations from other reducing sediments
585 (Canfield and Berner, 1987; Channell and Hawthorne, 1990; Nowaczyk, 2011). Other minerals were
586 completely encased by iron sulfides (**Figure 7d**). In elemental mapping, pitted regions of Fe-Ti oxides
587 often had higher Ti concentrations relative to Fe (**Figure 7a**). Pyrite framboids are common in all
588 samples, reaching tens of μm in size and formed with pyrite crystals typically between 1 and 2 μm
589 (**Figure 7e-g**).

590   In a single instance, a platy iron sulfide mineral was observed in the 148 cmbsf sample with
591 crystals about 1.5 – 2 μm in diameter (**Figure 7h**). We consider this tentative visual evidence for the
592 presence of fine-grained hexagonal 3C pyrrhotite in Core JKC36. We also observed a single instance of
593 an iron sulfide mineral framboid composed of crystals with a unique shape (**Figure 7i-k**). The crystals are
594 octahedral in shape and are about 0.5 – 1 μm in size. We consider this visual evidence for the presence
595 of fine-grained greigite (likely on the border between single domain and vortex state; Roberts et al.,
596 2011) in Core JKC36. However, magnetostatic interactions in greigite framboids could make their
597 magnetic signature appear like that of a larger, multi-domain particle (Valdez-Grijalva et al., 2020). For
598 both these minerals, the only major elements present are Fe and S, but we are unable to quantify the
599 ratio of the two elements for these unpolished samples. Given the presence of these iron sulfides with
600 large enough sizes to be imaged using an SEM, it is likely that there are additional, smaller iron sulfides
601 that are below the imaging capabilities of the SEM system.

602

603 4.2.6 Magnetic Mineralogy of Potential Source Rocks

604   To compare the Core JKC36 magnetic properties, particularly for the anomalous magnetic
605 mineral assemblage at 206 cmbsf, with potential source rock magnetic properties, magnetic
606 measurements from PRR rock samples that were available in the Joinville Island region were
607 investigated and indicate a wide range of magnetic grain sizes in the regional bedrock(**Figure 8**). The
608 samples with the highest M_s values are gabbros from small nearby islands. A Heroina Island gabbro (e.g.
609 Hamer and Hyden, 1984; Watts et al., 1984) has fine magnetic mineralogy (M_r/M_s = 0.38, H_{cr}/H_c = 1.66,

610   H_{cr} = 79.41, S-ratio = 0.99). A Wideopen Island gabbro has coarser magnetic mineralogy (M_r/M_s = 0.06,

611   H_{cr}/H_c = 2.63, H_{cr} = 6.86, S-ratio = 1.04) (**Figures 1 and 8**). χ_{lf} as a function of heating from room

612   temperature to ~700 °C in an argon atmosphere indicates that the magnetic mineralogy of these

613   samples is dominated by low titanium Fe-Ti oxides with χ_{lf} decreases between 500 and 580 °C for the

614   two samples (**Figure 8**).

615   Sedimentary and volcanic rocks from the Nordenskjöld Formation (e.g. Elliot, 1967;

616   Farquharson, 1983), Northern Joinville Island, have weaker M_s and relatively coarse magnetic grain size

617   (**Figures 1 and 8**). χ_{lf} curves as a function of heating from room temperature to ~700 °C are dominated by

618   steady declines that can be attributed to paramagnetic minerals and significant alteration creating

619   higher χ_{lf} above ~400 °C (**Figure 8**). One of the stronger Nordenskjöld Formation samples and the sample

620   with the finest magnetic mineralogy (M_r/M_s = 0.19, H_{cr}/H_c = 2.32, H_{cr} = 34.64, S-Ratio = 0.99) is an

621   andesite from King Point which has a steady magnetization decline between 500 and 600 °C, which

622   indicates a magnetic mineral assemblage consisting of low titanium Fe-Ti oxides (**Figure 8**).

623   A diorite sample from Mt. Alexander, southern Joinville Island (e.g. Grunow, 1993), has a

624   relatively fine magnetic mineralogy (M_r/M_s = 0.21, H_{cr}/H_c = 2.13, H_{cr} = 38.77, S-ratio = 0.82) (**Figures 1**

625   **and 8**). This sample has an abrupt χ_{lf} increase at ~235 °C and abrupt χ_{lf} decrease at 335 °C and 580 °C,

626   which indicate the cooccurrence of ferrimagnetic monoclinic 4C pyrrhotite and antiferromagnetic

627   hexagonal pyrrhotite polytypes (e.g. Rochette et al., 1990) and magnetite (**Figure 8**). Like the

628   Nordenskjöld Formation samples, the Mt. Alexander Diorite experiences significant alteration at high

629   temperatures, with χ_{lf} at room temperature after heating and cooling one order of magnitude larger

630   than the initial χ_{lf} measurement. While there is direct evident for pyrrhotite in this potential source rock,

631   the evidence is for pyrrhotite polytypes that are different from the hexagonal 3C pyrrhotite with room

632   temperature ferrimagnetic properties (Horng, 2018) that is most consistent with our rock magnetic data

633   from Core JKC36 (see **Figure 9** and discussion below).

634

5. Discussion

636

5.1 Magnetic Mineral Dissolution

638   Core JKC36 experiences significant detrital magnetic mineral dissolution through the SMT.

639   However, not all detrital iron-titanium-oxides are dissolved (**Figures 4 and 6**). Ferrimagnetic

640   (titano)magnetite steadily dissolves as $[S^{2-}]$ increases near the top of the SMT in the upper 30 cm of the

641   core (**Figure 3**) with dissolution preferentially removing stochiometric magnetite to titanomagnetite

642   (**Figure 4**) and finer (titano)magnetite to coarser (titano)magnetite (**Figures 5**). This is consistent with

643   previous observations and is likely related to stochiometric magnetite having a higher ratio of Fe^{3+} to Fe^{2+}

644   than titanomagnetite, and finer magnetic minerals having a higher surface area to volume ratio (Canfield

645   and Berner, 1987; Dillon and Bleil, 2006; Karlin, 1990). In the upper 30 cm, ferrimagnetic iron-titanium

646   oxide dissolution is accompanied by dissolution of iron-bearing paramagnetic minerals, which is tracked

647   by a decline in χ_{hf}, but not the dissolution of higher coercivity minerals (likely hematite) that are part of

648   the primary detrital assemblage, as indicated by no change in HIRM (**Figure 3**).

16

649   A dissolution front occurs between 30 and 32 cmbsf, where there is a large drop in parameters
650 sensitive to the concentration of (titano)magnetite (**Figure 3**). This dissolution front occurs in the upper
651 SMT, when sulfide is only at around one-third of its maximum observed value. Below the dissolution
652 front, (titano)magnetite dissolution is limited, likely due to the exhaustion of (titano)magnetite particles
653 that are susceptible to dissolution. High coercivity detrital minerals that contribute little to magnetic
654 remanence relative to (titano)magnetite begin to dissolve below the dissolution front and continue to
655 dissolve through the entire SMT where sulfide is elevated and below the depth of sulfate exhaustion.
656 These high-coercivity detrital components, likely hematite, are probably a source of ferric iron
657 throughout the SMT for microbial respiration.

658

5.2 Authigenic Magnetic Minerals 1: Superparamagnetic Enrichment

660   As previously observed in diagenetic sediments (Tarduno, 1995), there is clearly a SP mineral
661 enrichment within the SMT and in sediments below the SMT, as seen through H_c, H_{cr}/H_c, and frequency
662 dependent $\chi_{lf\text{-}MPMS}$ (**Figures 5 and 6**). This SP enrichment occurs in three stages, as follows.

1. Moving down core, the first signs of SP enrichment, as observed in the difference between the
   in-field H_c and remanence parameter H_{cr} and supported by frequency dependent $\chi_{lf\text{-}MPMS}$ (**Figures 5 and 6e**), occur just below the dissolution front in Zone 2a (33-87 cmbsf) where [Fe^{2+}] is
   depleted to background values, [SO_4^{2-}] is present, and [S^{2-}] is increasing downcore as it diffuses
   upward from the reduction of sulfate at around 80 cm (**Figures 2**). While not clear, SP
   enrichment is possibly also occurring above the dissolution front near the top of the SMT and is
   obscured by the relative coarsening of the detrital assemblage (**Figure 5**). SP enrichment in
   sulfate reducing sediments has previously been attributed to enrichment of fine-grained
   ferrimagnetic iron sulfides like greigite (Rowan et al., 2009). However, it is generally thought
   that preservation of minerals that form as intermediaries on the path to pyrite, like greigite,
   require sulfide limitation relative to iron to preserve the intermediary mineral (e.g. Kao et al.,
   2004), which is not the case here as S^{2-} is accumulating in the porewater during sulfate
   reduction, suggesting its production from sulfate is greater than its consumption from reacting
   with iron, and Fe^{2+} is not present in significant concentrations. While the nature of the Zone 2a
   SP enrichment is not clear at this time, we could be observing transient intermediary
   ferrimagnetic iron sulfides.
2. Below in Zone 2b (87-131 cmbsf), SP minerals are depleted relative to the overlying and
   underlying sediments, as indicated by lower H_{cr}/H_c (**Figure 5**). In this zone, sulfide decreases
   downcore in a concave-up shape, which suggests a continuous zone of consumption.
   Meanwhile, [Fe^{2+}] increases downcore to a local maximum near the base of Zone 2b, likely from
   iron reduction near the base of the SMT perhaps due to microbial iron reduction coupled to
   AOM (e.g. Beal et al., 2009; Riedinger et al., 2014). In Zone 2b, we also observe a χ_{hf} increase
   relative to Zone 2a sediments (**Figure 3**), which indicates that pyrite is being created and
   preserved at rates higher than iron-bearing paramagnetic minerals are being dissolved. The lack
   of SP minerals in Zone 2b is almost certainly the result of sufficient [Fe^{2+}] and [S^{2-}] in the
   porewater to let stable pyrite form without the preservation of SP ferrimagnetic iron sulfide
   intermediaries.
3. Near the top of Zone 3a (> 131 cmbsf), around the base of the SMT, we observe variable SP
   enrichment that is present to the base of the core, based on the range of H_{cr}/H_c variations

17

692   relative to Zone 2 (**Figure 5**). The top of Zone 3a is marked by a downcore decrease in sulfide to
693   negligible values below the SMT, which indicates consumption of sulfide that outpaces
694   production or diffusion now that we are far from where SO_4^{2-} is depleted. Fe^{2+} decreases
695   downcore which indicates dissolved iron production at rates faster than consumption by S^{2-} near
696   the base of the SMT. This likely creates conditions favorable for a $[S^{2-}]$-limitation relative to
697    $[Fe^{2+}]$, which allows preservation of ferrimagnetic iron sulfides that are intermediaries on the
698   pyrite formation pathway. These SP minerals are then likely preserved in the underlying
699   methanic sediments when $[S^{2-}]$ and $[Fe^{2+}]$ are depleted and at background levels. While we
700   cannot rule out the continued production of SP iron sulfides below this horizon near the base of
701   the SMT, we consider it likely that most of the SP minerals observed in the methanic sediments
702   beneath the SMT were formed at this horizon near the base of the SMT when porewater
703   conditions were favorable for their formation.

704

5.3 Authigenic Magnetic Minerals 2: Remanence-Bearing Iron Sulfides

706   Horizons with high concentrations of high coercivity minerals tracked by HIRM occur at a few
707   intervals, notably at 206 and 442 cmbsf (**Figure 3**). These horizons, which only occur at the bottom of the
708   SMT and below, have sharp bases that grade upward from high concentrations at the base to lower
709   concentrations above (**Figure 3**). High temperature χ_{lf} heating curves do not indicate any anomalous
710   magnetic minerals in these horizons (**Figure 4**). Perhaps this is not surprising because while these layers
711   are easy to pick out using remanence parameters, like M_r, HIRM, and H_{cr}, they cannot be distinguished
712   stratigraphically using in-field concentration dependent magnetic parameters like χ_{lf} and M_s (**Figures 3,
713   5**). These layers produce a looping pattern on a Day Plot (**Figure 5**), which has been interpreted as
714   diagnostic of greigite formation, with SP enrichment first pushing values to the right on the Day Plot and
715   then continued growth to stable single domain sizes pushing values toward the upper left-hand corner
716   (Rowan et al., 2009). However, the high remanence coercivity, tracked by H_{cr} values, and saturation
717   above 300 mT, tracked by low S-ratio values, is inconsistent with observations of sedimentary greigite
718   (Horng, 2018; Roberts et al., 2011). Thus, while authigenic greigite is likely present in the assemblage as
719   observed in SEM images (**Figure 7**), it cannot be the only mineral added to the altered detrital
720   assemblage observed elsewhere in the core below the SMT. We also consider significant hematite
721   concentrations unlikely because we see no indication of hematite in the high temperature χ_{lf} curves
722   given the amount of hematite required to lower the S-ratio to 0.87 (Frank and Nowaczyk, 2008).

723   The magnetic mineral that is most likely to explain our observation of high-coercivity horizons,
724   like the one that exists at the base of the SMT around 200 cm, is authigenic hexagonal 3C pyrrhotite.
725   Recent detailed documentation of rock magnetic properties from sedimentary hexagonal 3C pyrrhotite
726   nodules have challenged previous thoughts on authigenic pyrrhotite formation in sediments (Horng,
727   2018; Horng and Roberts, 2018). Comparison of our H_{cr} and S-ratio data with the observations of Horng
728   (2018) suggest that the high coercivity layers in Core JKC36 are likely a mixture of the altered detrital
729   assemblage and authigenic remanence bearing greigite and hexagonal 3C pyrrhotite (**Figure 9**). This is
730   consistent with the low temperature remanence data, IRM acquisition data, FORC diagrams, and SEM
731   observations (**Figures 6 and 7**). While monoclinic 4C pyrrhotite and an antiferromagnetic pyrrhotite
732   polytype is observed in the regional diorite bedrock sample, PRR16328 (**Figure 8**), the diorite's magnetic
733   properties are not similar to the magnetic properties of the high coercivity mineral horizon at 206 cmbsf
734   in JKC36 (**Figure 9**). This difference is expected because the pyrrhotite minerals found in the diorite have

18

735 different magnetic properties than authigenic hexagonal 3C pyrrhotite (Horng, 2018; Horng and Roberts,
736 2018). The relationship between H_{cr} and S-ratio in Zone 1 is different than the relationship in Zones 2
737 and 3 (**Figure 9c-d**), which suggests that the magnetic minerals driving S-ratio and HIRM variability are
738 largely different above the dissolution front versus below—which likely indicate that while in Zone 1
739 HIRM and S-ratio reflect the preferential dissolution of detrital (titano)magnetite relative to hematite, in
740 Zones 2 and 3 HIRM and S-ratio largely reflect the addition of authigenic hexagonal 3C pyrrhotite. The
741 trend of these samples in Zone 3 towards where the sedimentary 3C pyrrhotite nodules of Horng (2018)
742 plot is different from the trends that seem more typical of detrital assemblages, as observed above the
743 dissolution front in Zone 1; in more terrigenous Antarctic Peninsula Fjord glacial marine sediments with
744 less extreme diagenetic conditions (Reilly et al., 2016); in lake sediments that are interpreted to be a
745 mixture of magnetite and hematite (Stober and Thompson, 1979); and the regional bedrock samples
746 (**Figure 9**).

747   The largest of the high-coercivity layers occurs at the base of the SMT with its peak at 206
748 cmbsf, where $[S^{2-}]$ is almost completely depleted and below where $[Fe^{2+}]$ accumulates in the porewater
749 at the base of the SMT (**Figure 3**). We therefore hypothesize that this layer forms transiently at the
750 porewater transition where downward diffusing $[S^{2-}]$ is limited but there is still a source of $[Fe^{2+}]$, and
751 thus porewater conditions are favorable for the growth of remanence-bearing hexagonal 3C pyrrhotite
752 and greigite. The source of $[Fe^{2+}]$ following the complete reduction of sulfate may be AOM coupled to
753 microbial iron reduction (Beal et al., 2009; Riedinger et al., 2014). Microbial use of a ferric iron source
754 such as hematite could in part explain the slower dissolution rates of high-coercivity iron oxide
755 components of the detrital assemblage. In this case, the JKC36 206 cmbsf remanence-bearing layer is
756 created by the balance of $[Fe^{2+}]$ production by AOM coupled to microbial iron reduction and downward
757 $[S^{2-}]$ diffusion.

758   The formation of this transient remanence bearing iron sulfide layer at a redox boundary is
759 much like the formation of transient manganese oxide horizons near the top of the manganese
760 reduction zone, which are created by the balance of oxygen diffusing downward and Mn^{2+} diffusing
761 upward (Froelich et al., 1979). Thus, analogous to preserved manganese oxide layers (Froelich et al.,
762 1979), we predict that electron donor and/or organic carbon flux perturbations to steady state
763 diagenesis through the SMT should lead to preservation of horizons with high concentrations of
764 remanence-bearing hexagonal 3C pyrrhotite and greigite within the methanic zone such as the smaller
765 layer that peaks at 442 cmbsf (**Figures 3 and 5**).

766

5.4 Non-Steady State Diagenesis in Relation to Paleoenvironmental Conditions
768   There is evidence in Core JKC36 for non-steady state diagenesis over the time the sediments
769 were deposited, including a shift in magnetic mineral assemblage properties from Zone 3a to 3b around
770 325 cmbsf and preservation of a horizon with high concentrations of the remanence-bearing iron
771 sulfides, greigite and hexagonal 3C pyrrhotite, around 442 cmbsf (**Figures 3, 5, and 9**). Kyrmanidou et al.
772 (2018) observed an anomaly in the diatom assemblage over this time as well in the ratio of
773 *Chaetocerous subg*. *Hyalochaete* resting spores to cells (**Figure 10**). High concentrations of *Chaetocerous*
774 *subg*. *Hyalochaete* resting spores are generally interpreted as indicating high primary productivity during
775 the spring bloom (Buffen et al., 2007; Crosta et al., 1997; Leventer, 1991; Leventer et al., 1996, 2002).
776 *Chaetocerous subg*. *Hyalochaete* resting spores form as a survival mechanism when nutrients are

777 depleted after high primary productivity and low light during the polar winter following a large spring
778 bloom (Leventer et al., 1996; Crosta et al., 1997). A peak in the ratio of resting spores to cells between
779 about 150 and 275 cmbsf suggests that conditions in the late Holocene (~250-400 cal yrs BP) supported
780 higher primary productivity for a brief time.

781   If this primary productivity perturbation also led to increased organic matter export from the
782 surface ocean to the seafloor, the increased organic matter would fuel increased respiration of
783 sedimentary microbial communities and place a greater demand on electron acceptors, causing a shift in
784 the porewater geochemistry. To illustrate this idea, we offset the modern SMT to the core depth just
785 below the start of this primary productivity perturbation to conceptualize what the pore water profile
786 might have looked like at this time (**Figure 10**). This is a simplification that assumes other factors, such as
787 sedimentation rates, remain constant, which otherwise could drive non-steady state diagenesis itself.
788 However, this scenario is consistent with our observation that the depth of the transition from Zones 3a
789 to 3b between 300 and 350 cmbsf, which is marked by a M_s increase and H_{cr} decrease, is about where
790 we might expect the dissolution front to be at this time (solid gold line in **Figure 10**). Moreover, the
791 location of the deeper horizon of high concentration of remanence-bearing iron sulfide minerals around
792 442 cmbsf is around the base of this shifted SMT (dashed gold line in **Figure 10**). Therefore, we
793 hypothesize that this primary productivity perturbation increased the organic carbon supply to the
794 seafloor, which altered the porewater geochemistry including increasing the sulfide, leading to greater
795 magnetic mineral dissolution in Zone 3a relative to Zone 3b, and preserving a horizon of remanence-
796 bearing iron sulfides at the base of the pre-perturbation SMT.

797

6. Conclusions

799   We make new observations of magnetic mineral diagenesis in relation to porewater geochemistry in
800 a sedimentary record with a shallow SMT from Perseverance Drift, Northwestern Weddell Sea. While
801 more work is needed to investigate the kinetics of these processes, the following conclusions are
802 reached for our work.

803 - A (titano)magnetite dissolution front associated with elevated $[S^{2-}]$ in the upper portion of the
804   SMT occurs when $[S^{2-}]$ is about one-third of its peak concentration, almost 1 meter
805   stratigraphically above where sulfide reaches peak concentrations in the sediment porewater.
806 - During magnetic mineral dissolution, magnetite is preferentially dissolved relative to
807   titanomagnetite. While magnetite is exhausted in the upper part of the SMT, dissolution of
808   minerals with coercivity greater than 300 mT (likely hematite) continues through the entire SMT.
809   This could be an important source of ferric iron within the SMT.
810 - SP enrichment and depletion in this SMT occurs in three phases. First, when $[Fe^{2+}]$ is negligible
811   relative to $[S^{2-}]$ in the upper SMT where $[SO_4^{2-}]$ decreases downcore, SP minerals are enriched. SP
812   concentrations decrease in the zone below peak $[S^{2-}]$ concentrations, where the concave-up
813   shape of the sulfide profile indicates consumption, and $[Fe^{2+}]$ increases to above background
814   concentrations. These conditions are likely more favorable for pyrite formation than
815   ferrimagnetic iron sulfide formation. At the base of the SMT, where $[Fe^{2+}]$ is being produced or
816   diffused faster than it is consumed and $[S^{2-}]$ concentrations are low, SP minerals are enriched
817   again and preserved in the underlying methanic sediments.

818 • Horizons with high concentrations of high coercivity minerals that contribute significantly to the
819   bulk sediment remanent magnetization form at the base of the SMT where $[S^{2-}]$ is limited and
820     $[Fe^{2+}]$ is produced by iron reduction. During steady-state diagenesis, this horizon is likely
821   transient and moves with the SMT as sediment accumulates. Non-steady state diagenetic
822   changes driven by carbon flux or sedimentation rate changes could preserve these horizons in
823   the underlying methanic sediments. The magnetic properties of these horizons are consistent
824   with a mixture of an altered detrital magnetic mineral assemblage, greigite, and hexagonal 3C
825   pyrrhotite.
826 • Changes in the altered magnetic mineral assemblage preserved in the methanic zone are
827   consistent with changes in past porewater conditions and the nature of the SMT at the studied
828   site. This change to more extreme magnetic mineral diagenesis occurred following increased
829   primary productivity at Perseverance Drift and was likely a response to increased export
830   productivity to the seafloor. Non-steady state changes to porewater geochemistry likely led to
831   preservation of a high concentration of remanence-bearing iron sulfide horizon at depth in the
832   methanic zone that originally formed at the base of the paleo-SMT.

833

849

850

851 Figures

852

853 **Figure 1. Perseverance Drift regional map.** Left: Map of the Antarctic Peninsula with the Joinville Island
854 Study Area indicated with a red rectangle. Right: Location of Perseverance Drift, north of Joinville Island,
855 and sediment cores from Cruises LMG0404 (red) and NBP1203 (green) indicated. Polar Rock Repository
856 sample locations are also indicated (brown). Core JKC36 is the focus of this study.
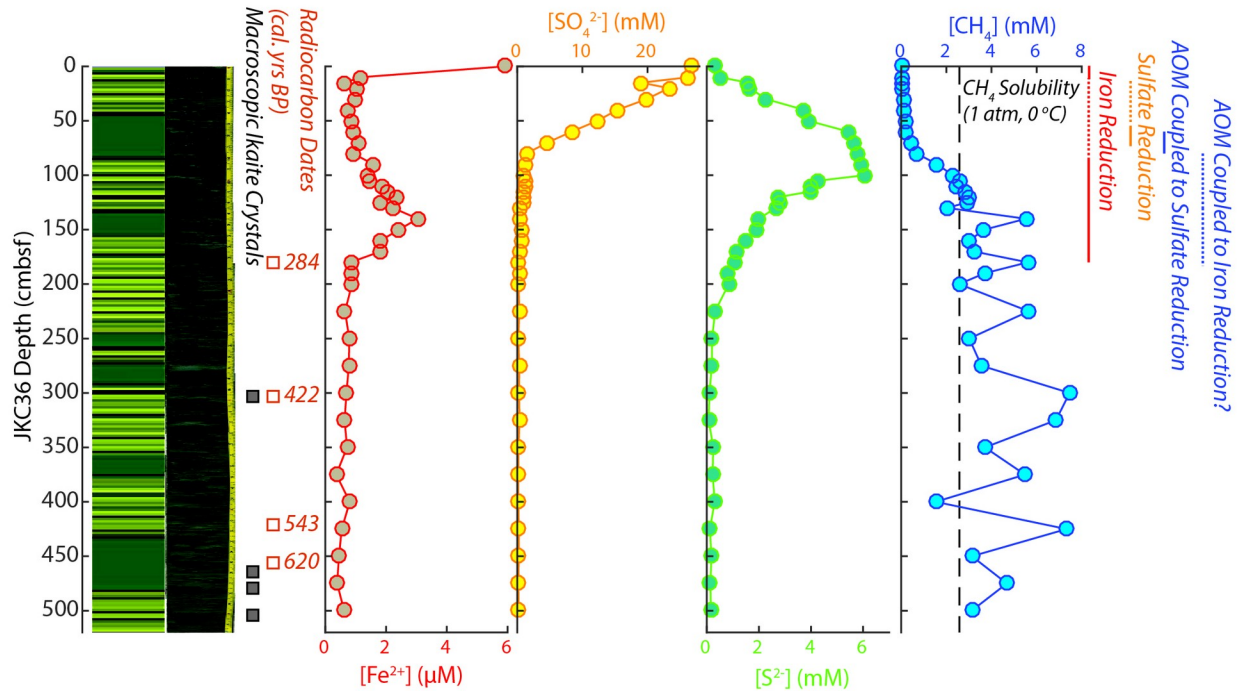
857

Figure 2. JKC36 stratigraphy and porewater geochemistry. From left to right: lithologic log indicating laminated (light green) versus bioturbated (dark green) intervals of JKC36 (Kyrmanidou et al., 2018); photograph of JKC36 (dark areas are where samples were taken for microbiology and porewater geochemistry immediately after recovery); brown squares indicate locations where macroscopic ikaite crystals were found; open orange squares indicate radiocarbon dates (corrected and calibrated in CALIB version 7.1 using ΔR = 860 yrs and the MARINE 13 dataset; Kyrmanidou et al., 2018); porewater dissolved ferrous iron (Fe^{2+} in red), sulfate (SO$_4^{2-}$ in gold), sulfide (S^{2-} in green), and methane (CH$_4$ in blue). Methane solubility at 1 atmosphere and 0 °C indicated with vertical dashed black line. Interpretation of porewater geochemistry included to the right (AOM = anaerobic oxidation of methane).
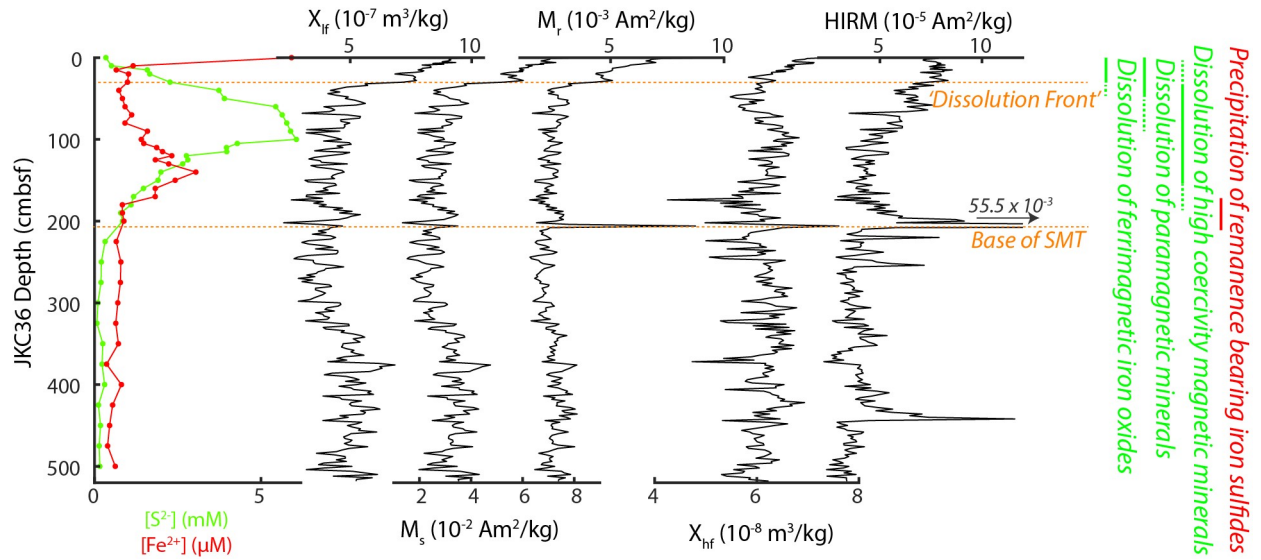
Figure 3. Concentration dependent magnetic parameters. From left to right: porewater S^{2-} (green) and Fe^{2+} (red) concentrations; low-field magnetic susceptibility (χ_{lf}); saturation magnetization (M_s); saturation remanence (M_r); high-field susceptibility (χ_{hf}); and the hard isothermal remanent magnetization (HIRM). The dissolution front around 30 cmbsf, where there is a sharp drop in χ_{lf}, M_s, and M_r, and the base of the sulfate-methane transition (SMT) around 200 cmbsf, where S^{2-} returns to background levels are indicated with horizontal dashed gold lines.

878
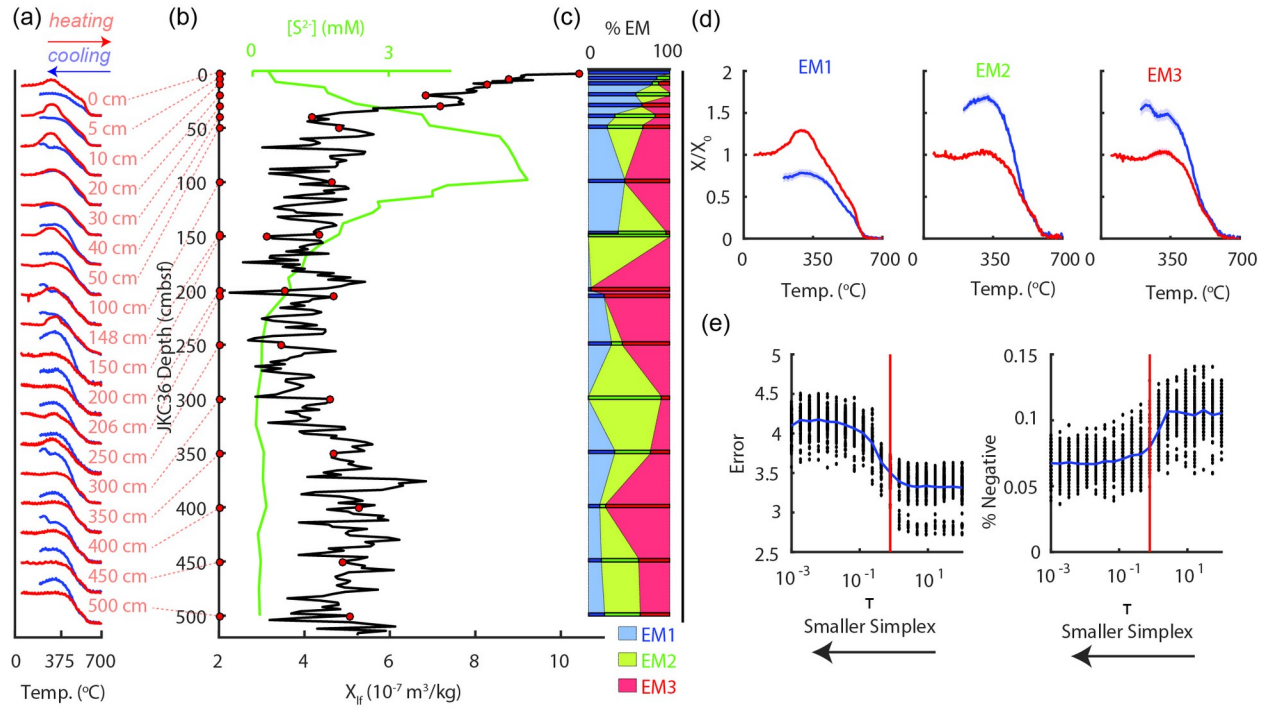
879 **Figure 4. JKC36 high temperature magnetic susceptibility. (a)** Magnetic susceptibility (χ_{lf}) as a function
880 of temperature for 18 horizons in JKC36. Red curves are measurements made while heating from room
881 temperature to about 700 °C and blue curves are measurements made while cooling from about 700 °C
882 back to room temperature. **(b)** Room temperature χ_{lf} (black) compared with the S^{2-} concentration in
883 JKC36 porewater (green). Horizons with χ_{lf} measurements as a function of temperature are indicated
884 with red dots. **(c)** Percent endmember 1 (blue), 2 (green), and 3 (red) from endmember modeling of the
885 temperature dependent χ_{lf} curves. **(d)** End member temperature dependent χ_{lf} curves (red = heating;
886 blue = cooling), with ±1 σ (shading). **(e)** End member model selection (vertical red line; τ = 0.7848) using
887 error (left) and shape constraints (right) for a range of regularization parameters (τ; see Reilly et al.
888 (2016) for discussion).

889

(a)

(b)

890

26
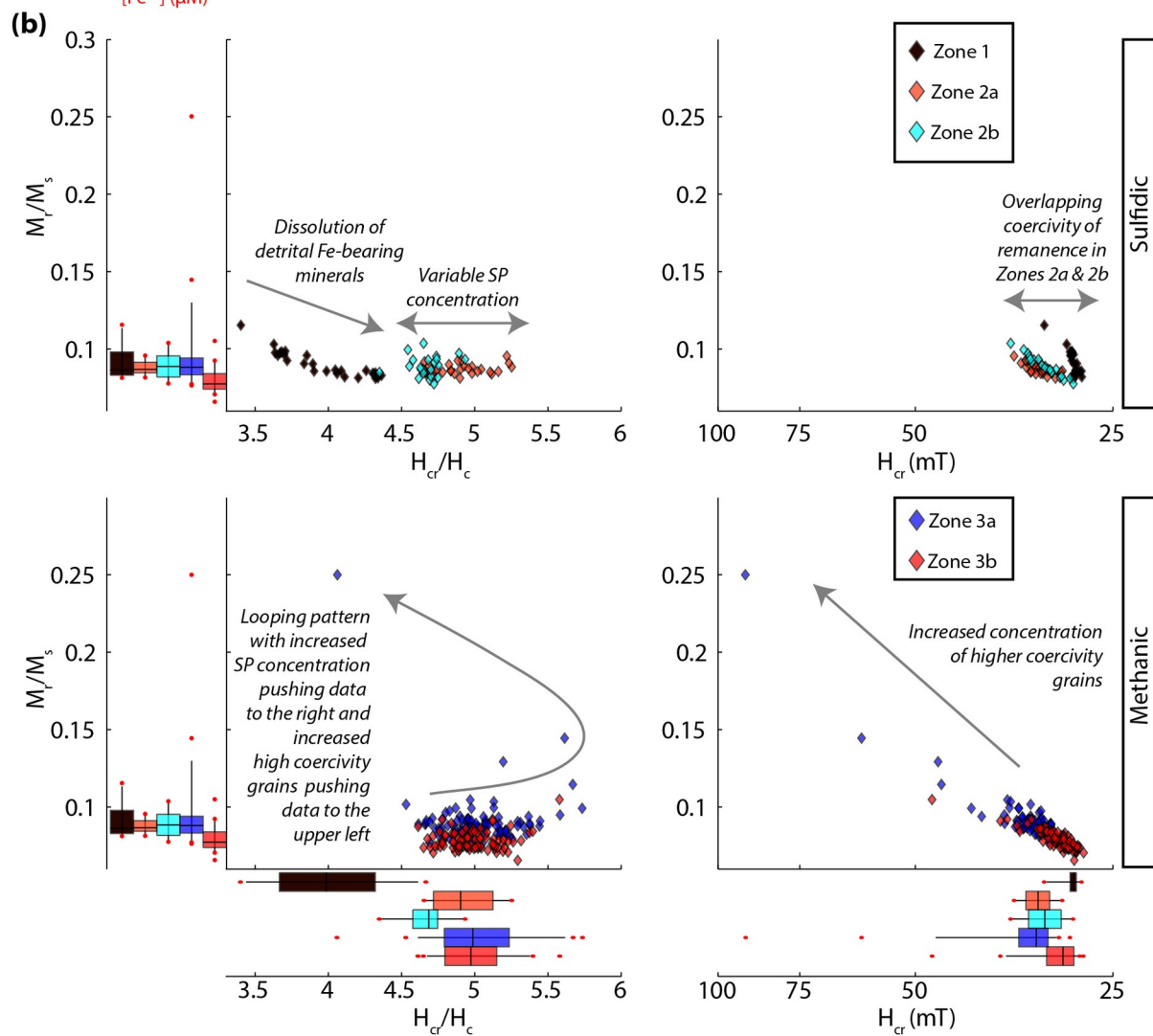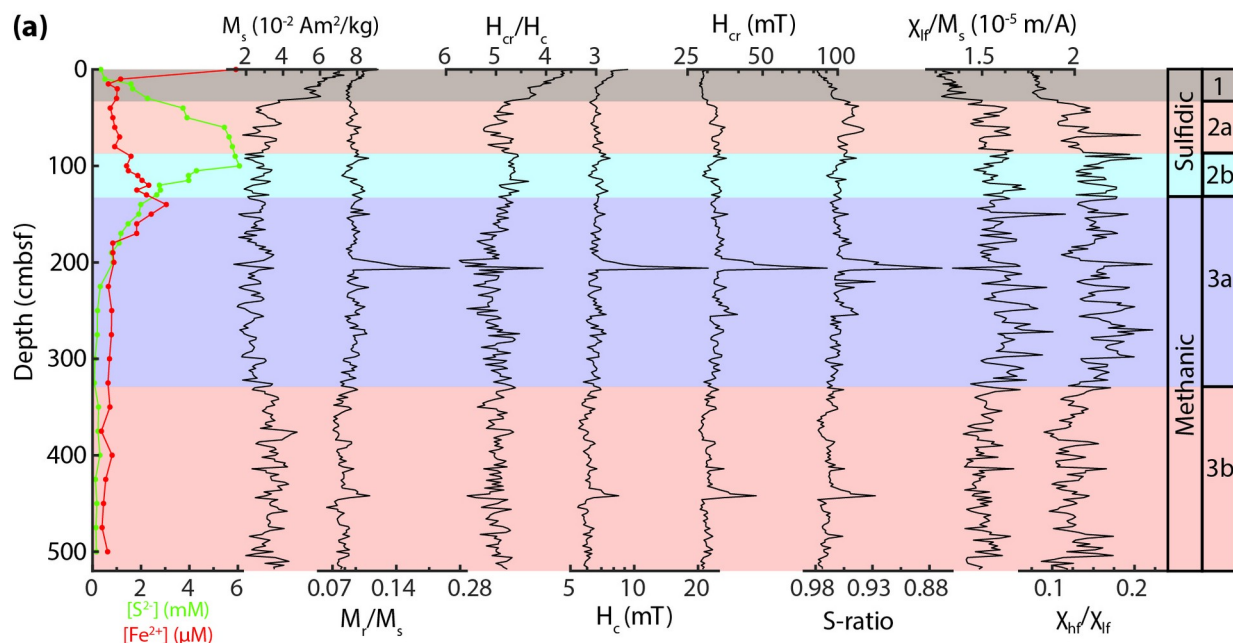
891 **Figure 5. JKC36 rock magnetic parameters. (a)** From left to right: porewater S^{2-} (green) and Fe^{2+} (red)
892 concentration; saturation magnetization (M_s); ratio of saturation remanence to saturation magnetization
893 (M_r/M_s); ratio of the coercivity of remanence to the bulk coercivity (H_{cr}/H_c); bulk coercivity (H_c);
894 coercivity of remanence (H_{cr}); the S-ratio; ratio of low-field magnetic susceptibility to saturation
895 magnetization (X_{lf}/M_s); ratio of high-field magnetic susceptibility to low field magnetic susceptibility ($X_{hf}/$
896 X_{lf}); and geochemical/magnetic zones discussed in the text. The dissolution front occurs at 33 cmbsf at
897 the base of Zone 1. The base of the SMT is in Zone 3a around 200 cmbsf. **(b)** Day Plots (Day et al., 1977)
898 and M_r/M_s plotted against H_{cr}. Box and whisker plots indicate the mean, the 84% percentile (box), and
899 the 95% percentile (whiskers). Data that plot outside of the 95% interval are indicated with red dots.
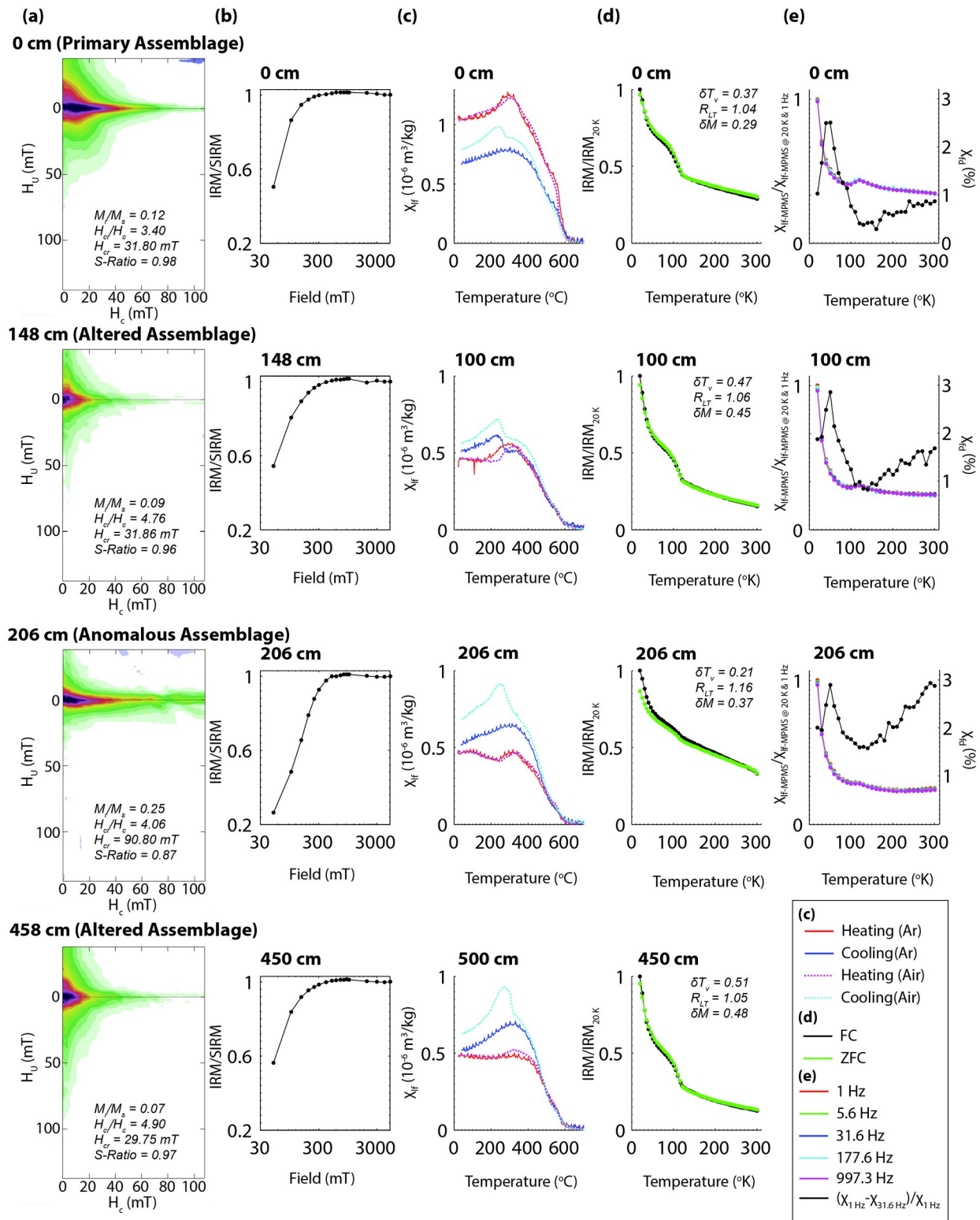
900

901

Figure 6. JKC36 rock magnetic investigations. (a) First order reversal curve (FORC) diagrams with
hysteresis and S-ratio parameters listed. **(b)** Isothermal remanent magnetization (IRM) acquisition
curves normalized by the IRM at 1000 mT (SIRM). **(c)** Comparison of magnetic susceptibility (χ_{lf}) as a

905   function of temperature when measured in an argon atmosphere (solid line) compared to ambient air
906   (dashed lines). **(d)** Comparison of field cooled (FC) and zero field cooled (ZFC) IRMs. **(e)** Low temperature
907   magnetic susceptibility ($\chi_{lf\text{-}MPMS}$) measured with five frequencies (colored lines). Frequency dependent
908   low temperature magnetic susceptibility (χ_{fd}; black line).

909

910

911
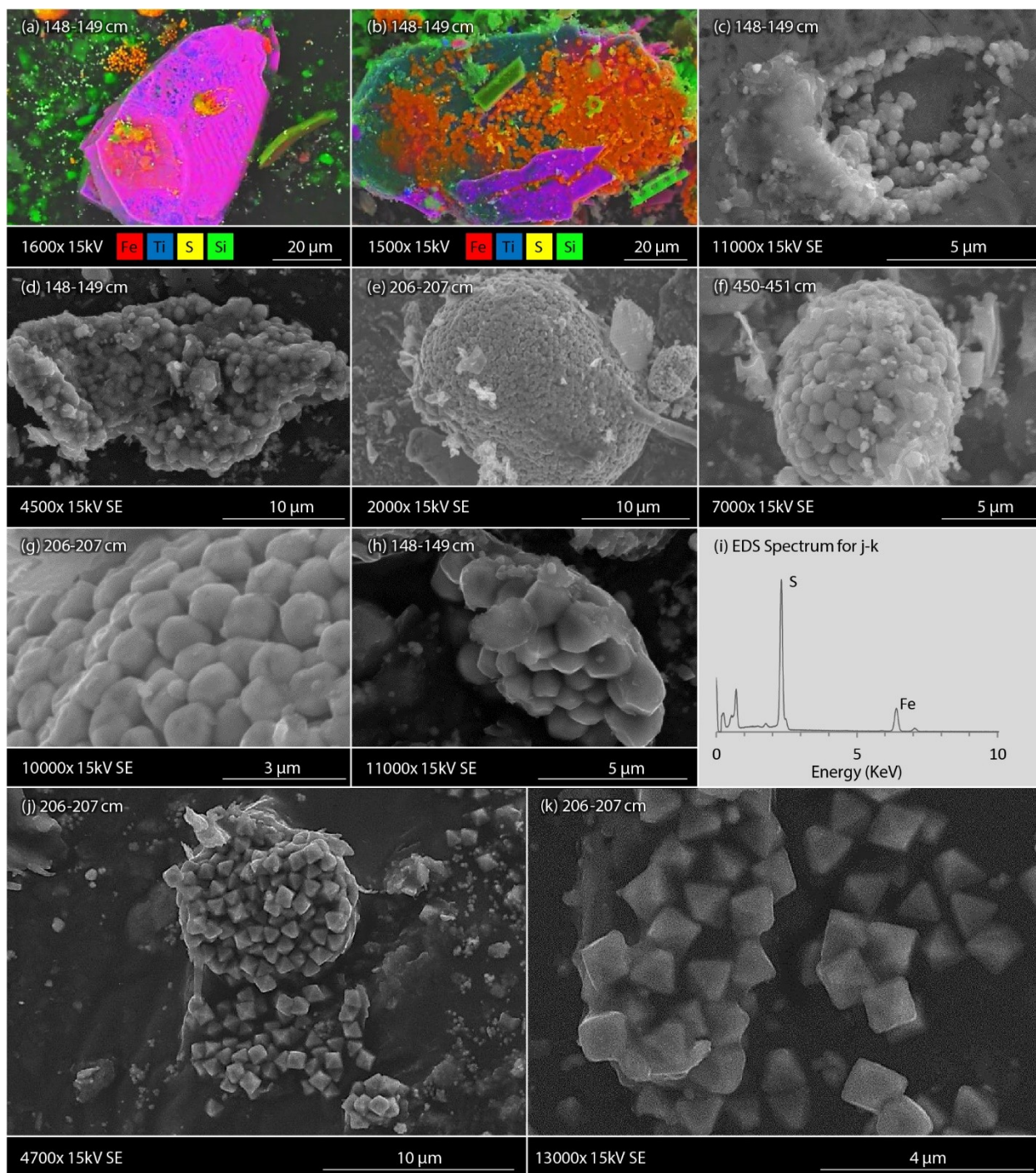
Figure 7. JKC36 SEM images. (a-d) Examples of dissolution of iron bearing minerals and growth of
authigenic iron sulfides. **(e-g)** Examples of pyrite framboids. **(h)** Example of an iron sulfide mineral with
platy mineral structure that is tentatively interpreted as hexagonal 3C pyrrhotite. **(i)** EDS spectrum for
iron sulfide mineral displayed in **(j-k)**. **(j-k)** Example of iron sulfide mineral with octahedral crystal
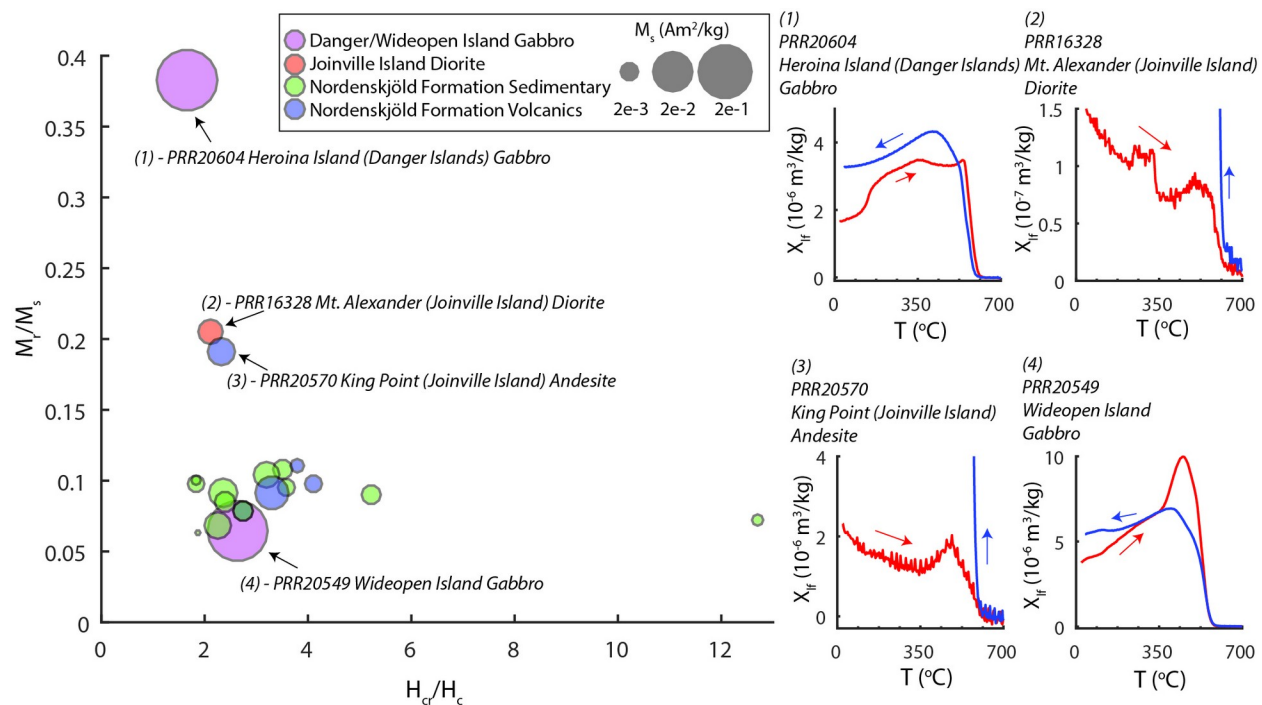structure consistent with greigite.

918

Figure 8. Potential source rocks. (Left) Day plot (Day et al., 1977) for Polar Rock Repository (PRR) samples from the Joinville Island region. The size of the circle is proportional to the M_s of the sample. All Nordenskjöld Formation samples are from Northern Joinville Island, while the Joinville Island Diorite is from southern Joinville Island (Figure 1). (Right) Selected χ_{lf} measurements as a function of heating to ~700 °C and cooling back to room temperature in an argon atmosphere. Samples not plotted have low χ_{lf} and were dominated by paramagnetic contributions and significant alteration above 400 °C, but all data are available in the MagIC Database (see Acknowledgements).
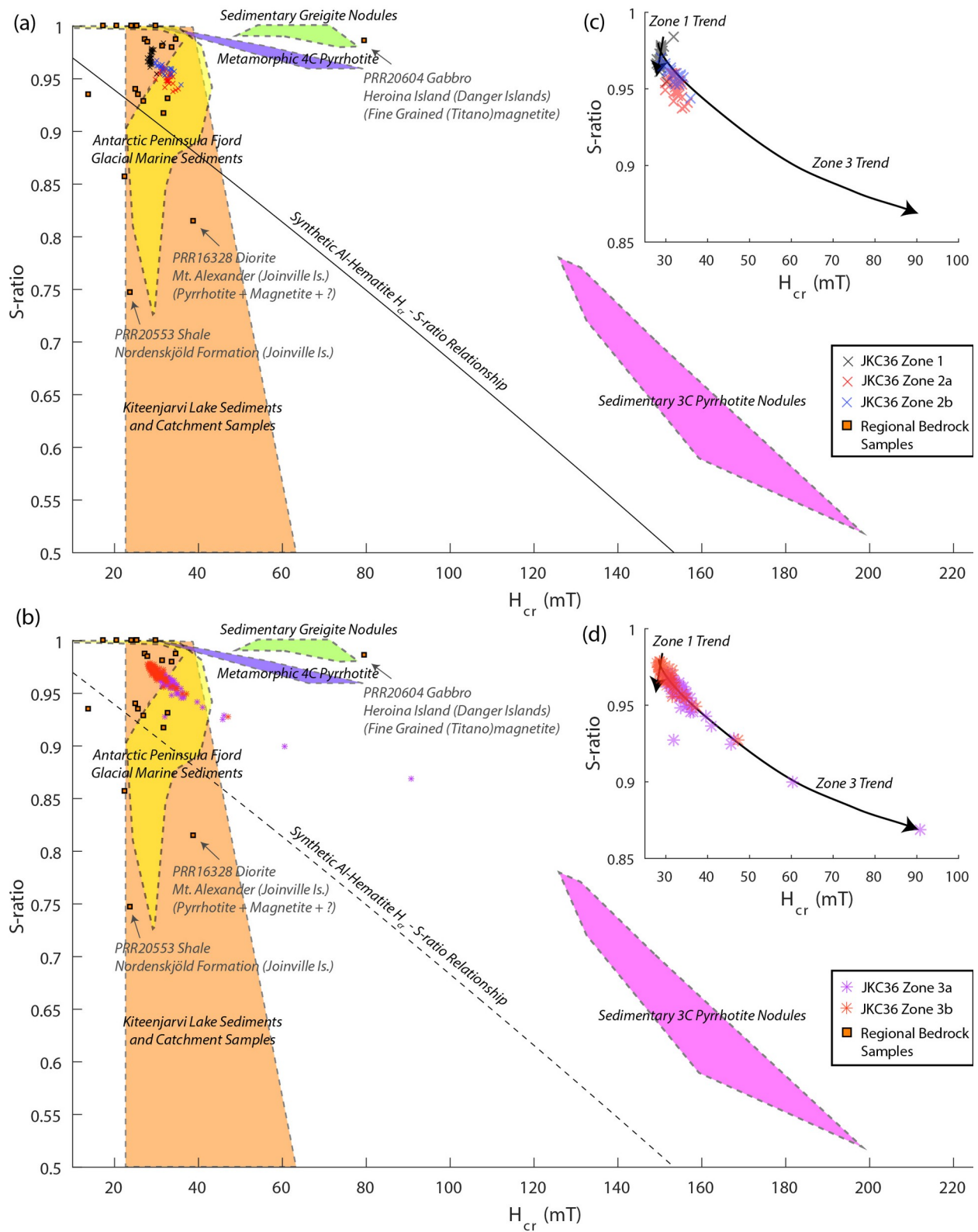
Figure 9. Comparison of Coercivity of Remanence (H_{cr}) and S-ratio. Core JKC36 H_{cr} and S-ratio values for
(a) sulfidic sediments and **(b)** methanic sediments compared with regional bedrock samples (squares),

930   values from glacial marine sediments in Barilari Bay, Western Antarctic Peninsula (yellow shading; Reilly

931   et al., 2016), mixed hematite and magnetite magnetic mineral assemblages from Kiteenjarvi Lake and its

932   catchment (orange shading; Stober and Thompson, 1979), and ranges for sedimentary hexagonal 3C

933   pyrrhotite nodules (pink shading), sedimentary greigite nodules (green shading), and metamorphic rock

934   monoclinic 4C pyrrhotite (purple shading) (Horng, 2018). The relationship between H_{cr} and S-ratio for

935   synthetic Al-hematite samples is also plotted (black dashed line; Liu et al., 2007). **(c-d)** Expanded view of

936   the Core JKC36 data, annotated with trend lines for the Zone 1 and Zone 3 samples.
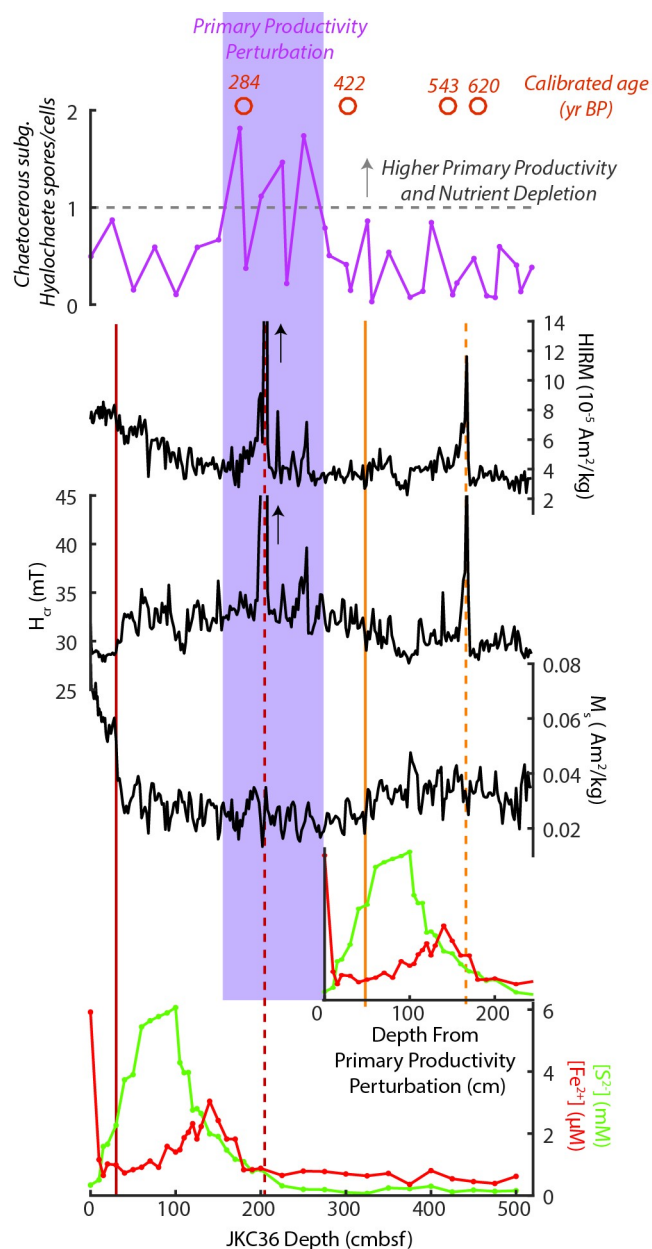
937

Figure 10. Comparison to Past Primary Productivity. From bottom to top: Porewater sulfide and iron concentrations measured in Core JKC36; porewater data shifted 275 cm to represent what porewater conditions may have looked like before a late Holocene primary productivity increase; M_s; H_{cr}; HIRM; ratio of *Chaetocerous subg. Hyalochaete* resting spores to cells (Kyrmanidou et al., 2018); and radiocarbon dates ($\Delta R = 860$ yrs; Kyrmanidou et al., 2018). A primary productivity perturbation based on diatom data is highlighted in purple. The red solid vertical line indicates the modern dissolution front while the red dashed vertical line indicates the modern base of the SMT where high concentrations of remanence-bearing iron sulfides accumulate. Vertical orange solid and dashed lines indicate the hypothetical locations of the same two horizons about 400 cal. yrs ago prior to a perturbation caused by increased primary productivity. Note the vertical orange solid line is at about the depth separating Zones

949   3a and 3b (Figure 5) and the vertical orange dashed line is where there is an enrichment of high
950   coercivity minerals at 442 cmbsf.

References

Beal, E.J., House, C.H., Orphan, V.J., 2009. Manganese- and iron-dependent marine methane oxidation. Science 325, 184–187. https://doi.org/10.1126/science.1169984

Berner, R.A., 1984. Sedimentary pyrite formation: An update. Geochimica et Cosmochimica Acta 48, 605–615. https://doi.org/10.1016/0016-7037(84)90089-9

Berner, R.A., 1970. Sedimentary pyrite formation. American Journal of Science 268, 1–23. https://doi.org/10.2475/ajs.268.1.1

Bioucas-Dias, J.M., 2009. A variable splitting augmented Lagrangian approach to linear spectral unmixing, in: First Workshop on Hyperspectral Image and Signal Processing: Evolution in Remote Sensing, 2009. WHISPERS '09. Presented at the First Workshop on Hyperspectral Image and Signal Processing: Evolution in Remote Sensing, 2009. WHISPERS '09, pp. 1–4. https://doi.org/10.1109/WHISPERS.2009.5289072

Blanchet, C.L., Thouveny, N., Vidal, L., 2009. Formation and preservation of greigite (Fe_3S_4) in sediments from the Santa Barbara Basin: Implications for paleoenvironmental changes during the past 35 ka. Paleoceanography 24, PA2224. https://doi.org/10.1029/2008PA001719

Brachfeld, S., Barletta, F., St-Onge, G., Darby, D., Ortiz, J.D., 2009. Impact of diagenesis on the environmental magnetic record from a Holocene sedimentary sequence from the Chukchi–Alaskan margin, Arctic Ocean. Global and Planetary Change 68, 100–114. https://doi.org/10.1016/j.gloplacha.2009.03.023

Brachfeld, S.A., 2006. High-field magnetic susceptibility (χHF) as a proxy of biogenic sedimentation along the Antarctic Peninsula. Physics of the Earth and Planetary Interiors 156, 274–282. https://doi.org/10.1016/j.pepi.2005.06.019

Buffen, A., Leventer, A., Rubin, A., Hutchins, T., 2007. Diatom assemblages in surface sediments of the northwestern Weddell Sea, Antarctic Peninsula. Marine Micropaleontology 62, 7–30. https://doi.org/10.1016/j.marmicro.2006.07.002

Canfield, D.E., 1989. Reactive iron in marine sediments. Geochimica et Cosmochimica Acta 53, 619–632. https://doi.org/10.1016/0016-7037(89)90005-7

Canfield, D.E., Berner, R.A., 1987. Dissolution and pyritization of magnetite in anoxic marine sediments. Geochimica et Cosmochimica Acta 51, 645–659.

Carter–Stiglitz, B., Moskowitz, B., Solheid, P., Berquó, T.S., Jackson, M., Kosterov, A., 2006. Low-temperature magnetic behavior of multidomain titanomagnetites: TM0, TM16, and TM35. Journal of Geophysical Research: Solid Earth 111. https://doi.org/10.1029/2006JB004561

Carvallo, C., R.Muxworthy, A., J.Dunlop, D., 2006. First-order reversal curve (FORC) diagrams of magnetic mixtures: Micromagnetic models and measurements. Physics of the Earth and Planetary Interiors, Developments in Techniques and Methods Related to Rock Magnetism 154, 308–322. https://doi.org/10.1016/j.pepi.2005.06.017

987   Chang, L., Bolton, C. T., Dekkers, M. J., Hayashida, A., Heslop, D., Krijgsman, W., et al. 2016a. Asian
988   monsoon modulation of nonsteady state diagenesis in hemipelagic marine sediments offshore
989   of Japan. Geochemistry, Geophysics, Geosystems, 17(11), 4383–4398.
990   https://doi.org/10.1002/2016GC006344

991   Chang, L., Roberts, A.P., Heslop, D., Hayashida, A., Li, J., Zhao, X., Tian, W., Huang, Q., 2016b.
992   Widespread occurrence of silicate-hosted magnetic mineral inclusions in marine sediments and
993   their contribution to paleomagnetic recording. Journal of Geophysical Research: Solid Earth 121,
994   2016JB013109. https://doi.org/10.1002/2016JB013109

995   Chang, L., Roberts, A.P., Rowan, C.J., Tang, Y., Pruner, P., Chen, Q., Horng, C.-S., 2009. Low-temperature
996   magnetic properties of greigite (Fe_3S_4). Geochemistry, Geophysics, Geosystems 10.
997   https://doi.org/10.1029/2008GC002276

998   Chang, L., Roberts, A.P., Tang, Y., Rainford, B.D., Muxworthy, A.R., Chen, Q., 2008. Fundamental
999   magnetic parameters from pure synthetic greigite (Fe3S4). Journal of Geophysical Research:
1000   Solid Earth 113. https://doi.org/10.1029/2007JB005502

1001   Channell, J.E.T., Hawthorne, T., 1990. Progressive dissolution of titanomagnetites at ODP Site 653
1002   (Tyrrhenian Sea). Earth and Planetary Science Letters 96, 469–480.
1003   https://doi.org/10.1016/0012-821X(90)90021-O

1004   Cline, J.D., 1969. Spectrophotometric determination of hydrogen sulfide in natural waters 1. Limnology
1005   and Oceanography 14, 454–458. https://doi.org/10.4319/lo.1969.14.3.0454

1006   Crosta, X., Pichon, J.-J., Labracherie, M., 1997. Distribution of Chaetoceros resting spores in modern peri-
1007   Antarctic sediments. Marine Micropaleontology 29, 283–299. https://doi.org/10.1016/S0377-
1008   8398(96)00033-3

1009   Darley, R., 2014. Geochemical and rock-magnetic analyses of Kasten cores and surface grab samples
1010   from the Joinville-D'Urville Trough, northeastern Antarctic Peninsula: Results and correlation
1011   with the western Antarctic Peninsula (M.S. Thesis). Montclair State University.

1012   Day, R., Fuller, M., Schmidt, V., 1977. Hysteresis properties of titanomagnetites: Grain size and
1013   compositional dependence. Physics of the Earth and Planetary Interiors 13, 260–267.

1014   Dillon, M., Bleil, U., 2006. Rock magnetic signatures in diagenetically altered sediments from the Niger
1015   deep-sea fan. Journal of Geophysical Research: Solid Earth 111.
1016   https://doi.org/10.1029/2004JB003540

1017   Domack, E., Halverson, G., Willmott, V., Leventer, A., Brachfeld, S., Ishman, S., 2007. Spatial and
1018   temporal distribution of ikaite crystals in Antarctic glacial marine sediments. USGS Open-File
1019   Report 1047.

1020   Domack, E., the LMG0404 Scientific Party, 2004. *L.M. Gould 2004-04* Cruise Report: 16 April - 11 May.

1021   Egli, R., 2013. VARIFORC: An optimized protocol for calculating non-regular first-order reversal curve
1022   (FORC) diagrams. Global and Planetary Change, 110, 302–320.
1023   https://doi.org/10.1016/j.gloplacha.2013.08.003

1024   Elliot, D.H., 1967. The geology of Joinville Island, British Antarctic Survey Bulletin, 12, pp. 23-40.

1025   Farquharson, G.W., 1983. The Nordenskjöld Formation of the northern Antarctic Peninsula: An Upper
1026   Jurassic radiolarian mudstone and tuff sequence. British Antarctic Survey Bulletin 60, 1–22.

1027   Frank, U., Nowaczyk, N.R., 2008. Mineral magnetic properties of artificial samples systematically mixed
1028   from haematite and magnetite. Geophysical Journal International 175, 449–461. https://doi.org/
1029   10.1111/j.1365-246X.2008.03821.x

1030   Froelich, P.N., Klinkhammer, G.P., Bender, M.L., Luedtke, N.A., Heath, G.R., Cullen, D., Dauphin, P.,
1031   Hammond, D., Hartman, B., Maynard, V., 1979. Early oxidation of organic matter in pelagic
1032   sediments of the eastern equatorial Atlantic: Suboxic diagenesis. Geochimica et Cosmochimica
1033   Acta 43, 1075–1090.

1034   Garming, J.F.L., Bleil, U., Riedinger, N., 2005. Alteration of magnetic mineralogy at the sulfate–methane
1035   transition: Analysis of sediments from the Argentine continental slope. Physics of the Earth and
1036   Planetary Interiors 151, 290–308. https://doi.org/10.1016/j.pepi.2005.04.001

1037   Gehring, A.U., Fischer, H., Louvel, M., Kunze, K., Weidler, P.G., 2009. High temperature stability of
1038   natural maghemite: A magnetic and spectroscopic study. Geophysical Journal International 179,
1039   1361–1371. https://doi.org/10.1111/j.1365-246X.2009.04348.x

1040   Grunow, A.M., 1993. New paleomagnetic data from the Antarctic Peninsula and their tectonic
1041   implications. Journal of Geophysical Research: Solid Earth 98, 13815–13833.
1042   https://doi.org/10.1029/93JB01089

1043   Hamer, R.D., Hyden, G., 1984. The geochemistry and age of the Danger Islands pluton, Antarctic
1044   Peninsula. British Antarctic Survey Bulletin 64, 1–19.

1045   Harrison, R.J., Feinberg, J.M., 2008. FORCinel: An improved algorithm for calculating first-order reversal
1046   curve distributions using locally weighted regression smoothing. Geochemistry, Geophysics,
1047   Geosystems. 9, Q05016. https://doi.org/10.1029/2008GC001987

1048   Harrison, R.J., Muraszko, J., Heslop, D., Lascu, I., Muxworthy, A.R., Roberts, A.P., 2018. An improved
1049   algorithm For unmixing first−order reversal curve diagrams using principal component analysis.
1050   Geochemistry, Geophysics, Geosystems. https://doi.org/10.1029/2018GC007511

1051   Hatfield, R.G., Stoner, J.S., Reilly, B.T., Tepley, F.J., Wheeler, B.H., Housen, B.A., 2017. Grain size
1052   dependent magnetic discrimination of Iceland and South Greenland terrestrial sediments in the
1053   northern North Atlantic sediment record. Earth and Planetary Science Letters 474, 474–489.
1054   https://doi.org/10.1016/j.epsl.2017.06.042

1055   Heslop, D., Roberts, A.P., 2012. A method for unmixing magnetic hysteresis loops. Journal of Geophysical
1056   Research: Solid Earth 117, B3. https://doi.org/10.1029/2011JB008859

1057   Horng, C.-S., 2018. Unusual magnetic properties of sedimentary pyrrhotite in methane seepage
1058   sediments: Comparison with metamorphic pyrrhotite and sedimentary greigite. Journal of
1059   Geophysical Research: Solid Earth 123, 4601–4617. https://doi.org/10.1002/2017JB015262

1060   Horng, C.-S., Roberts, A.P., 2018. The low-temperature Besnus magnetic transition: Signals due to
1061   monoclinic and hexagonal pyrrhotite. Geochemistry, Geophysics, Geosystems 19, 3364–3375.
1062   https://doi.org/10.1029/2017GC007394

1063   Hunger, S., Benning, L.G., 2007. Greigite: A true intermediate on the polysulfide pathway to pyrite.
1064   Geochemical Transactions 8, 1. https://doi.org/10.1186/1467-4866-8-1

1065   Jiang, W.-T., Horng, C.-S., Roberts, A.P., Peacor, D.R., 2001. Contradictory magnetic polarities in
1066   sediments and variable timing of neoformation of authigenic greigite. Earth and Planetary
1067   Science Letters 193, 1–12. https://doi.org/10.1016/S0012-821X(01)00497-6

1068   Kao, S.-J., Horng, C.-S., Roberts, A.P., Liu, K.-K., 2004. Carbon–sulfur–iron relationships in sedimentary
1069   rocks from southwestern Taiwan: Influence of geochemical environment on greigite and
1070   pyrrhotite formation. Chemical Geology 203, 153–168.
1071   https://doi.org/10.1016/j.chemgeo.2003.09.007

1072   Karlin, R., 1990. Magnetite diagenesis in marine sediments from the Oregon continental margin. Journal
1073   of Geophysical Research: Solid Earth 95, 4405–4419.

1074   Karlin, R., Levi, S., 1983. Diagenesis of magnetic minerals in recent haemipelagic sediments. Nature 303,
1075   327–330.

1076   Kars, M., Kodama, K., 2015. Authigenesis of magnetic minerals in gas hydrate-bearing sediments in the
1077   Nankai Trough, offshore Japan. Geochemistry, Geophysics, Geosystems 16, 947–961.
1078   https://doi.org/10.1002/2014GC005614

1079   Kars, M., Musgrave, R.J., Hoshino, T., Jonas, A.-S., Bauersachs, T., Inagaki, F., Kodama, K., 2018. Magnetic
1080   Mineral Diagenesis in a High Temperature and Deep Methanic Zone in Izu Rear Arc Marine
1081   Sediments, Northwest Pacific Ocean. Journal of Geophysical Research: Solid Earth 123, 8331–
1082   8348. https://doi.org/10.1029/2018JB015861

1083   Knittel, K., Boetius, A., 2009. Anaerobic Oxidation of Methane: Progress with an Unknown Process.
1084   Annual Review of Microbiology 63, 311–334.
1085   https://doi.org/10.1146/annurev.micro.61.080706.093130

1086   Kuehl, S.A., Nittrouer, C.A., DeMaster, D.J., Curtin, T.B., 1985. A long, square-barrel gravity corer for
1087   sedimentological and geochemical investigation of fine-grained sediments. Marine Geology 62,
1088   365–370. https://doi.org/10.1016/0025-3227(85)90124-0

1089   Kyrmanidou, A., Vadman, K.J., Ishman, S.E., Leventer, A., Brachfeld, S., Domack, E.W., Wellner, J.S., 2018.
1090   Late Holocene oceanographic and climatic variability recorded by the Perseverance Drift,
1091   northwestern Weddell Sea, based on benthic foraminifera and diatoms. Marine
1092   Micropaleontology 141, 10–22. https://doi.org/10.1016/j.marmicro.2018.03.001

1093   Larrasoaña, J.C., Roberts, A.P., Musgrave, R.J., Gràcia, E., Piñero, E., Vega, M., Martínez-Ruiz, F., 2007.
1094   Diagenetic formation of greigite and pyrrhotite in gas hydrate marine sedimentary systems.
1095   Earth and Planetary Science Letters 261, 350–366. https://doi.org/10.1016/j.epsl.2007.06.032

1096   Larrasoaña, J.C., Roberts, A.P., Stoner, J.S., Richter, C., Wehausen, R., 2003. A new proxy for bottom-
1097   water ventilation in the eastern Mediterranean based on diagenetically controlled magnetic

1098   properties of sapropel-bearing sediments. Palaeogeography, Palaeoclimatology, Palaeoecology
1099   190, 221–242. https://doi.org/10.1016/S0031-0182(02)00607-7

1100   Lattard, D., Engelmann, R., Kontny, A., Sauerzapf, U., 2006. Curie temperatures of synthetic
1101   titanomagnetites in the Fe-Ti-O system: Effects of composition, crystal chemistry, and
1102   thermomagnetic methods. Journal of Geophysical Research 111.
1103   https://doi.org/10.1029/2006JB004591

1104   Lavoie, C., Domack, E.W., Pettit, E.C., Scambos, T.A., Larter, R.D., Schenke, H.-W., Yoo, K.C., Gutt, J.,
1105   Wellner, J., Canals, M., Anderson, J.B., Amblas, D., 2015. Configuration of the Northern Antarctic
1106   Peninsula Ice Sheet at LGM based on a new synthesis of seabed imagery. The Cryosphere 9,
1107   613–629. https://doi.org/10.5194/tc-9-613-2015

1108   Leslie, B.W., Hammond, D.E., Berelson, W.M., Lund, S.P., 1990. Diagenesis in anoxic sediments from the
1109   California continental borderland and its influence on iron, sulfur, and magnetite behavior.
1110   Journal of Geophysical Research 95, 4453–4470.

1111   Leventer, A., 1991. Sediment trap diatom assemblages from the northern Antarctic Peninsula region.
1112   Deep Sea Research Part A. Oceanographic Research Papers 38, 1127–1143.
1113   https://doi.org/10.1016/0198-0149(91)90099-2

1114   Leventer, A., Domack, E., Barkoukis, A., McAndrews, B., Murray, J., 2002. Laminations from the Palmer
1115   Deep: A diatom-based interpretation. Paleoceanography 17, PAL 3-1-PAL 3-15.
1116   https://doi.org/10.1029/2001PA000624

1117   Leventer, A., Domack, E.W., Ishman, S.E., Brachfeld, S.A., McClennen, C.E., Manley, P., 1996. 200-300
1118   year productivity cycles in the Antarctic Peninsula region: Understanding linkages among the
1119   Sun, atmosphere, oceans, sea-ice and biota, Geological Society of America Bulletin 108, 1626-
1120   1644. https://doi.org/10.1130/0016-7606(1996)108<1626:PCOYIT>2.3.CO;2

1121   Liu, J., Zhu, R., Roberts, A.P., Li, S., Chang, J.-H., 2004. High-resolution analysis of early diagenetic effects
1122   on magnetic minerals in post-middle-Holocene continental shelf sediments from the Korea
1123   Strait. Journal of Geophysical Research: Solid Earth 109. https://doi.org/10.1029/2003JB002813

1124   Liu, P., Hirt, A.M., Schüler, D., Uebe, R., Zhu, P., Liu, T., Zhang, H., 2019. Numerical unmixing of weakly
1125   and strongly magnetic minerals: Examples with synthetic mixtures of magnetite and hematite.
1126   Geophysical Journal International. https://doi.org/10.1093/gji/ggz022

1127   Liu, Q., Roberts, A.P., Larrasoaña, J.C., Banerjee, S.K., Guyodo, Y., Tauxe, L., Oldfield, F., 2012.
1128   Environmental magnetism: Principles and applications. Reviews of Geophysics 50.
1129   https://doi.org/10.1029/2012RG000393

1130   Liu, Q., Roberts, A.P., Torrent, J., Horng, C.-S., Larrasoaña, J.C., 2007. What do the HIRM and S-ratio
1131   really measure in environmental magnetism? Geochemistry, Geophysics, Geosystems 8. https://
1132   doi.org/10.1029/2007GC001717

1133   Lu, Z., Rickaby, R.E.M., Kennedy, H., Kennedy, P., Pancost, R.D., Shaw, S., Lennie, A., Wellner, J.,
1134   Anderson, J.B., 2012. An ikaite record of late Holocene climate at the Antarctic Peninsula. Earth
1135   and Planetary Science Letters 325–326, 108–115. https://doi.org/10.1016/j.epsl.2012.01.036

1136   Moskowitz, B.M., Frankel, R.B., Bazylinski, D.A., 1993. Rock magnetic criteria for the detection of
1137   biogenic magnetite. Earth and Planetary Science Letters 120, 283–300.
1138   https://doi.org/10.1016/0012-821X(93)90245-5

1139   Moskowitz, B.M., Jackson, M., Kissel, C., 1998. Low-temperature magnetic behavior of titanomagnetites.
1140   Earth and Planetary Science Letters 157, 141–149. https://doi.org/10.1016/S0012-
1141   821X(98)00033-8

1142   Nowaczyk, N.R., 2011. Dissolution of titanomagnetite and sulphidization in sediments from Lake
1143   Kinneret, Israel. Geophys J Int 187, 34–44. https://doi.org/10.1111/j.1365-246X.2011.05120.x

1144   Özdemir, Ö., Banerjee, S.K., 1984. High temperature stability of maghemite (γ-Fe2O3). Geophysical
1145   Research Letters 11, 161–164. https://doi.org/10.1029/GL011i003p00161

1146   Özdemir, Ö., Dunlop, D.J., Moskowitz, B.M., 1993. The effect of oxidation on the Verwey transition in
1147   magnetite. Geophysical Research Letters 20, 1671–1674. https://doi.org/10.1029/93GL01483

1148   Pike, C.R., Roberts, A.P., Verosub, K.L., 1999. Characterizing interactions in fine magnetic particle
1149   systems using first order reversal curves. Journal of Applied Physics 85, 6660–6667.
1150   https://doi.org/10.1063/1.370176

1151   Reilly, B.T., Natter, C.J., Brachfeld, S.A., 2016. Holocene glacial activity in Barilari Bay, west Antarctic
1152   Peninsula, tracked by magnetic mineral assemblages: Linking ice, ocean, and atmosphere.
1153   Geochemistry Geophysics Geosystems 17. https://doi.org/10.1002/2016GC006627

1154   Riedinger, N., Formolo, M.J., Lyons, T.W., Henkel, S., Beck, A., Kasten, S., 2014. An inorganic geochemical
1155   argument for coupled anaerobic oxidation of methane and iron reduction in marine sediments.
1156   Geobiology 12, 172–181. https://doi.org/10.1111/gbi.12077

1157   Roberts, A.P., 2015. Magnetic mineral diagenesis. Earth-Science Reviews 151, 1–47.
1158   https://doi.org/10.1016/j.earscirev.2015.09.010

1159   Roberts, A.P., Chang, L., Rowan, C.J., Horng, C.-S., Florindo, F., 2011. Magnetic properties of sedimentary
1160   greigite (Fe_3S_4): An update. Reviews of Geophysics 49. https://doi.org/10.1029/2010RG000336

1161   Roberts, A.P., Liu, Q., Rowan, C.J., Chang, L., Carvallo, C., Torrent, J., Horng, C.-S., 2006. Characterization
1162   of hematite (α-Fe_2O_3), goethite (α-FeOOH), greigite (Fe_3S_4), and pyrrhotite (Fe_7S_8) using first-
1163   order reversal curve diagrams. Journal of Geophysical Research: Solid Earth 111. https://doi.org/
1164   10.1029/2006JB004715

1165   Roberts, A.P., Tauxe, L., Heslop, D., Zhao, X., Jiang, Z., 2018a. A critical appraisal of the "Day" diagram.
1166   Journal of Geophysical Research: Solid Earth 0. https://doi.org/10.1002/2017JB015247

1167   Roberts, A.P., Zhao, X., Harrison, R.J., Heslop, D., Muxworthy, A.R., Rowan, C.J., Larrasoaña, J.-C.,
1168   Florindo, F., 2018b. Signatures of reductive magnetic mineral diagenesis from unmixing of first-
1169   order reversal curves. Journal of Geophysical Research: Solid Earth 123, 4500–4522.
1170   https://doi.org/10.1029/2018JB015706

1171 Rochette, P., Fillion, G., Mattéi, J.-L., Dekkers, M.J., 1990. Magnetic transition at 30–34 Kelvin in
1172   pyrrhotite: Insight into a widespread occurrence of this mineral in rocks. Earth and Planetary
1173   Science Letters 98, 319–328. https://doi.org/10.1016/0012-821X(90)90034-U

1174 Rowan, C.J., Roberts, A.P., 2006. Magnetite dissolution, diachronous greigite formation, and secondary
1175   magnetizations from pyrite oxidation: Unravelling complex magnetizations in Neogene marine
1176   sediments from New Zealand. Earth and Planetary Science Letters 241, 119–137.
1177   https://doi.org/10.1016/j.epsl.2005.10.017

1178 Rowan, C.J., Roberts, A.P., Broadbent, T., 2009. Reductive diagenesis, magnetite dissolution, greigite
1179   growth and paleomagnetic smoothing in marine sediments: A new view. Earth and Planetary
1180   Science Letters 277, 223–235. https://doi.org/10.1016/j.epsl.2008.10.016

1181 Schwarz, E.J., Vaughan, D.J., 1972. Magnetic phase relations of Pyrrhotite. Journal of geomagnetism
1182   geoelectricity 24, 441–458. https://doi.org/10.5636/jgg.24.441

1183 Skipp, G., Brownfield, I.K., 1993. Improved density gradient separation techniques using sodium
1184   polytungstate and a comparison to the use of other heavy liquids. US Department of the
1185   Interior, US Geological Survey Denver, CO.

1186 Smirnov, A.V., 2009. Grain size dependence of low-temperature remanent magnetization in natural and
1187   synthetic magnetite: Experimental study. Earth, Planets and Space 61, BF03352891.
1188   https://doi.org/10.1186/BF03352891

1189 Spielhagen, R.F., Tripati, A., 2009. Evidence from Svalbard for near-freezing temperatures and climate
1190   oscillations in the Arctic during the Paleocene and Eocene. Palaeogeography, Palaeoclimatology,
1191   Palaeoecology 278, 48–56. https://doi.org/10.1016/j.palaeo.2009.04.012

1192 Stober, J.C., Thompson, R., 1979. An investigation into the source of magnetic minerals in some Finnish
1193   lake sediments. Earth and Planetary Science Letters 45, 464–474. https://doi.org/10.1016/0012-
1194   821X(79)90145-6

1195 Stoner, J.S., Channell, J.E.T., Hillaire-Marcel, C., 1996. The magnetic signature of rapidly deposited
1196   detrital layers from the deep Labrador Sea: Relationship to North Atlantic Heinrich layers.
1197   Paleoceanography 11, 309–325.

1198 Stookey, L.L., 1970. Ferrozine---a new spectrophotometric reagent for iron. Analytical Chemistry 42,
1199   779–781. https://doi.org/10.1021/ac60289a016

1200 Suess, E., Balzer, W., Hesse, K.-F., Müller, P.J., Ungerer, C.A., Wefer, G., 1982. Calcium carbonate
1201   hexahydrate from organic-rich sediments of the Antarctic Shelf: Precursors of glendonites.
1202   Science 216, 1128–1131. https://doi.org/10.1126/science.216.4550.1128

1203 Sweeney, R.E., Kaplan, I.R., 1973. Pyrite framboid formation; Laboratory synthesis and marine
1204   sediments. Economic Geology 68, 618–634. https://doi.org/10.2113/gsecongeo.68.5.618

1205 Tarduno, J.A., 1995. Superparamagnetism and reduction diagenesis in pelagic sediments: enhancement
1206   or depletion? Geophysical Research Letters 22, 1337–1340.

1207   Tarduno, J.A., 1994. Temporal trends of magnetic dissolution in the pelagic realm: Gauging
1208   paleoproductivity? Earth and Planetary Science Letters 123, 39–48.

1209   Valdez-Grijalva, M.A., Nagy, L., Muxworthy, A.R., Williams, W., Roberts, A.P., Heslop, D., 2020.
1210   Micromagnetic simulations of first-order reversal curve (FORC) diagrams of framboidal greigite.
1211   Geophys J Int 222, 1126–1134. https://doi.org/10.1093/gji/ggaa241

1212   Vernet, M., the NBP1203 Scientific Party, 2012. *N.B. Palmer 2012-03* Cruise Report: 11 March - 19 April.

1213   Walz, F., Torres, L., Bendimya, K., de Francisco, C., Kronmüller, H., 1997. Analysis of magnetic after-effect
1214   spectra in titanium-doped magnetite. Physica Status Solidi (a) 164, 805–820.
1215   https://doi.org/10.1002/1521-396X(199712)164:2<805::AID-PSSA805>3.0.CO;2-N

1216   Watts, D.R., Watts, G.C., Bramall, A.M., 1984. Cretaceous and Early Tertiary paleomagnetic results from
1217   the Antarctic Peninsula. Tectonics 3, 333–346. https://doi.org/10.1029/TC003i003p00333

1218   Wellner, J., Scambos, T., Domack, E., Vernet, M., Leventer, A., Balco, G., Brachfeld, S., Cape, M., Huber,
1219   B., Ishman, S., McCormick, M., Mosley-Thompson, E., Pettit, E., Smith, C., Truffer, M., Van Dover,
1220   C., Yoo, K.-C., 2019. The Larsen Ice Shelf System, Antarctica (LARISSA): Polar systems bound
1221   together, changing fast. GSA Today. https://doi.org/10.1130/GSATG382A.1

1222   Worm, H.-U., 1998. On the superparamagnetic—stable single domain transition for magnetite, and
1223   frequency dependence of susceptibility. Geophysical Journal International 133, 201–206.
1224   https://doi.org/10.1046/j.1365-246X.1998.1331468.x

1225   Worm, H.-U., Jackson, M., 1999. The superparamagnetism of Yucca Mountain Tuff. Journal of
1226   Geophysical Research: Solid Earth 104, 25415–25425. https://doi.org/10.1029/1999JB900285

1227   Yamamoto, S., Alcauskas, J.B., Crozier, T.E., 1976. Solubility of methane in distilled water and seawater.
1228   Journal of Chemical and Engineering Data 21, 78–80.

1229   Yamazaki, T., Abdeldayem, A.L., Ikehara, K., 2003. Rock-magnetic changes with reduction diagenesis in
1230   Japan Sea sediments and preservation of geomagnetic secular variation in inclination during the
1231   last 30,000 years. Earth Planets and Space 55, 327–340. https://doi.org/10.1186/BF03351766

1232   Zhou, X., Lu, Z., Rickaby, R.E.M., Domack, E.W., Wellner, J.S., Kennedy, H.A., 2015. Ikaite abundance
1233   controlled by porewater phosphorus level: Potential links to dust and productivity. The Journal
1234   of Geology 123, 269–281. https://doi.org/10.1086/681918

1235